# TOI 762 A b AND TIC 46432937 b: TWO GIANT PLANETS TRANSITING M DWARF STARS

Joel D. Hartman,[1] Daniel Bayliss,[2,3] Rafael Brahm,[4,5,6] Edward M. Bryant,[7] Andrés Jordán,[4,5,6]
Gáspár Á. Bakos,[1] Melissa J. Hobson,[8] Elyar Sedaghati,[9] Xavier Bonfils,[10] Marion Cointepas,[10,8]
Jose Manuel Almenara,[10,8] Khalid Barkaoui,[11,12,13] Mathilde Timmermans,[11] George Dransfield,[14]
Elsa Ducrot,[15,16] Sebastián Zúñiga-Fernández,[11] Matthew J. Hooton,[17] Peter Pihlmann Pedersen,[17]
Francisco J. Pozuelos,[18] Amaury H. M. J. Triaud,[14] Michaël Gillon,[11] Emmanuel Jehin,[19]
William C. Waalkes,[20] Zachory K. Berta-Thompson,[21] Steve B. Howell,[22] Elise Furlan,[23] George R. Ricker,[24]
Roland Vanderspek,[24] Sara Seager,[24,25,26] Joshua N. Winn,[1] Jon M. Jenkins,[22] David Rapetti,[22,27]
Karen A. Collins,[28] David Charbonneau,[28] Christopher J. Burke,[24] and David R. Rodriguez[29]

[1] *Department of Astrophysical Sciences, Princeton University, 4 Ivy Lane, Princeton, NJ 08544, USA*

[2] *Dept. of Physics, University of Warwick, Gibbet Hill Road, Coventry CV4 7AL, UK*

[3] *Centre for Exoplanets and Habitability, University of Warwick, Gibbet Hill Road, Coventry CV4 7AL, UK*

[4] *Millennium Institute of Astrophysics (MAS), Nuncio Monseñor Sótero Sanz 100, Providencia, Santiago, Chile*

[5] *Facultad de Ingeniería y Ciencias, Universidad Adolfo Ibáñez, Av. Diagonal las Torres 2640, Peñalolén, Santiago, Chile*

[6] *Data Observatory Foundation, Santiago, Chile*

[7] *Mullard Space Science Laboratory, University College London, Holmbury St Mary, Dorking, RH5 6NT, UK*

[8] *Observatoire de Genève, Département d'Astronomie, Université de Genève, Chemin Pegasi 51b, 1290 Versoix, Switzerland*

[9] *European Southern Observatory (ESO), Av. Alonso de Córdova 3107, 763 0355 Vitacura, Santiago, Chile*

[10] *Univ. Grenoble Alpes, CNRS, IPAG, F-38000 Grenoble, France*

[11] *Astrobiology Research Unit, Université de Liège, Allée du 6 Août 19C, B-4000 Liège, Belgium*

[12] *Department of Earth, Atmospheric and Planetary Science, Massachusetts Institute of Technology, 77 Massachusetts Avenue, Cambridge, MA 02139, USA*

[13] *Instituto de Astrofísica de Canarias (IAC), Calle Vía Láctea s/n, 38200, La Laguna, Tenerife, Spain*

[14] *School of Physics & Astronomy, University of Birmingham, Edgbaston, Birmingham B15 2TT, UK*

[15] *Paris Region Fellow, Marie Sklodowska-Curie Action*

[16] *AIM, CEA, CNRS, Université Paris-Saclay, Université de Paris, F-91191 Gif-sur-Yvette, France*

[17] *Cavendish Laboratory, JJ Thomson Avenue, Cambridge CB3 0HE, UK*

[18] *Instituto de Astrofísica de Andalucía (IAA-CSIC), Glorieta de la Astronomía s/n, 18008 Granada, Spain*

[19] *Space Sciences, Technologies and Astrophysics Research (STAR) Institute, Université de Liège, Allée du 6 Août 19C, B-4000 Liège, Belgium*

[20] *Department of Physics and Astronomy, Dartmouth College, Hanover NH 03755, USA*

[21] *Department of Astrophysical & Planetary Sciences, University of Colorado Boulder, Boulder CO 80309, USA*

[22] *NASA Ames Research Center, Moffett Field, CA 94035, USA*

[23] *NASA Exoplanet Science Institute, Caltech/IPAC, Mail Code 100-22, 1200 E. California Blvd., Pasadena, CA 91125, USA*

[24] *Department of Physics and Kavli Institute for Astrophysics and Space Research, Massachusetts Institute of Technology, Cambridge, MA 02139, USA*

[25] *Department of Earth, Atmospheric and Planetary Sciences, Massachusetts Institute of Technology, Cambridge, MA 02139, USA*

[26] *Department of Aeronautics and Astronautics, MIT, 77 Massachusetts Avenue, Cambridge, MA 02139, USA*

[27] *Research Institute for Advanced Computer Science, Universities Space Research Association, Washington, DC 20024, USA*

[28] *Center for Astrophysics | Harvard & Smithsonian, 60 Garden Street, Cambridge, MA 02138, USA*

[29] *Space Telescope Science Institute, 3700 San Martin Drive, Baltimore, MD, 21218, USA*

## ABSTRACT

Corresponding author: Joel Hartman

jhartman@astro.princeton.edu

arXiv:2407.07187v1 [astro-ph.EP] 9 Jul 2024

We present the discovery of TOI 762 A b and TIC 46432937 b, two giant planets transiting M dwarf stars. Transits of both systems were first detected from observations by the NASA *TESS* mission, and the transiting objects are confirmed as planets through high-precision radial velocity (RV) observations carried out with VLT/ESPRESSO. TOI 762 A b is a warm sub-Saturn with a mass of $0.251 \pm 0.042 \, M_{\rm J}$, a radius of $0.744 \pm 0.017 \, R_{\rm J}$, and an orbital period of 3.4717 d. It transits a mid-M dwarf star with a mass of $0.442 \pm 0.025 \, M_{\odot}$ and a radius of $0.4250 \pm 0.0091 \, R_{\odot}$. The star TOI 762 A has a resolved binary star companion TOI 762 B that is separated from TOI 762 A by $3\rlap{.}''2$ ($\sim 319 \, {\rm AU}$) and has an estimated mass of $0.227 \pm 0.010 \, M_{\odot}$. The planet TIC 46432937 b is a warm Super-Jupiter with a mass of $3.20 \pm 0.11 \, M_{\rm J}$ and radius of $1.188 \pm 0.030 \, R_{\rm J}$. The planet's orbital period is $P = 1.4404$ d, and it undergoes grazing transits of its early M dwarf host star, which has a mass of $0.563 \pm 0.029 \, M_{\odot}$ and a radius of $0.5299 \pm 0.0091 \, R_{\odot}$. TIC 46432937 b is one of the highest mass planets found to date transiting an M dwarf star. TIC 46432937 b is also a promising target for atmospheric observations, having the highest Transmission Spectroscopy Metric or Emission Spectroscopy Metric value of any known warm Super-Jupiter (mass greater than $3.0 \, M_{\rm J}$, equilibrium temperature below 1000 K).

# 1. INTRODUCTION

How do the properties of giant planets depend on the masses of their host stars? This is a key open question and topic of current research in the field of exoplanets. Efforts to address this question have been limited by the relatively small number of low-mass and high-mass stars that have been searched for planets compared to the much larger sample of Solar-mass stars that have been searched to date by surveys like *Kepler* (Borucki et al. 2010) and *TESS* (Ricker et al. 2015).

In order to expand the sample of giant planets known around low-mass stars, we have been carrying out a program to follow-up candidate transiting giant planets around M dwarf stars and late K dwarf stars using the ESPRESSO instrument on the 8 m Very Large Telescope (VLT) at Paranal Observatory, in Chile. This facility has proven to be very efficient at gathering high-precision RV observations for faint stars, even down to $V \sim 16.5$. We have so far published the confirmation of seven systems through this effort (Hartman et al. 2020; Jordán et al. 2022; Hobson et al. 2023; Almenara et al. 2023), and in this paper we publish the confirmation of two more such objects.

The planets that we confirm in this paper were identified by the NASA *TESS* mission, which has been carrying out a wide-field search for transiting planets around bright stars since its launch in 2018. Thanks to its all-sky observing strategy, the mission has also been successful at discovering the rare instances of transiting giant planets ($M_p > 0.1\,M_J$, for discussion purposes) around M dwarf stars. A total of 17 of the 20 transiting giant planets that have been confirmed around M dwarf stars so far were either first identified by *TESS*, or included *TESS* follow-up observations as part of the discovery (Bakos et al. 2020; Cañas et al. 2020, 2022, 2023; Gan et al. 2022, 2023; Hartman et al. 2023; Hobson et al. 2023; Jordán et al. 2022; Kagetani et al. 2023; Kanodia et al. 2021, 2022, 2023; Triaud et al. 2023). The three other known systems were discovered by *Kepler* (Johnson et al. 2012), HATSouth (Hartman et al. 2015) and NGTS (Bayliss et al. 2018).

While *TESS* has been very successful at discovering giant planets around M dwarfs, many of these objects were not identified through the mission's primary transit search effort operated by the Science Processing Operations Center (SPOC; Jenkins et al. 2016) at NASA Ames Research Center (ARC), which focuses on the 2 min cadence observations, but were instead identified through special efforts to produce light curves for faint M dwarf stars from the Full Frame Images (FFIs) and to search them for transit signals. One such effort is the *TESS* Faint-star search (Kunimoto et al. 2022), which

has identified some 3200 faint *TESS* Objects of Interest (TOIs) to date, including 128 candidate giant planets transiting M dwarfs. Another example is Bryant et al. (2023) who conducted a search for transiting giant planets around M dwarfs in 30 min cadence *TESS* observations and identified 15 candidates, including 7 that were not previously identified by other projects. Both of the planets that we confirm in this paper were included in the Bryant et al. (2023) sample, and one of these systems (TIC 46432937 b) was first identified by them.

In the following section we discuss the observations that are used to confirm and characterize each planetary system. In Section 3 we describe the analysis methods. In Section 4 we discuss the results.

# 2. OBSERVATIONS

## 2.1. *Initial Photometric Detection*

Both TOI 762 A b and TIC 46432937 b were first identified as transiting planet candidates from observations gathered by the NASA *TESS* mission. Table 2 summarizes the *TESS* observations that are available for each system. Both targets were identified as candidates by an independent transit search performed by Bryant et al. (2023) with the aim of measuring the occurrence rates of giant planets with low-mass host stars. For this search the Box-fitting Least Squares (BLS; Kovács et al. 2002) algorithm was utilised to search for giant planets transiting low-mass stars in light curves generated from the 30 minute cadence Full-Frame-Images (FFIs) from Cycle 1 of the *TESS* mission by the TESS-SPOC team (Caldwell et al. 2020). During Cycle 1 both TOI 762 A b and TIC 46432937 b were observed in a single sector: Sector 10 for TOI 762 A b (2019 Mar 29–2019 Apr 22) and Sector 6 for TIC 46432937 b (2018 Dec 15–2019 Jan 6). Following the BLS detection of these two candidates a number of automated checks were performed to investigate whether the transit-like signals could be the result of a number of different false positive scenarios, such as eclipsing binaries or variable stars. See Bryant et al. (2023) for more details on the analyses performed. For both TOI 762 A b and TIC 46432937 b we found no evidence that the transit-like signals were a result of a non-planetary scenario. An initial transit fitting analysis was performed on both candidates using the BATMAN package (Kreidberg 2015) to generate the transit models and using EMCEE (Foreman-Mackey et al. 2013) to perform the MCMC sampling. Both objects were identified as high likelihood giant planet candidates by this analysis and included in the sample reported in Bryant et al. (2023).

TOI 762 A b was independently identified as a candidate by the *TESS* Science Processing Operations Cen-

ter (SPOC; Jenkins et al. 2016) at NASA ARC. The SPOC conducted a transit search of Sector 10 on 23 May 2019 with an adaptive, noise-compensating matched filter (Jenkins 2002; Jenkins et al. 2010, 2020), producing a threshold crossing event (TCE) for which an initial limb-darkened transit model was fitted (Li et al. 2019) and a suite of diagnostic tests were conducted to help make or break the planetary nature of the signal (Twicken et al. 2018). The transit signature was also detected in a search of FFI data by the Quick Look Pipeline (QLP) at MIT (Huang et al. 2020a,b). The TESS Science Office (TSO) reviewed the vetting information and issued an alert on 27 February 2020 (Guerrero et al. 2021). The signal was repeatedly recovered as additional observations were made in Sectors 36, 37, and 63, and the transit signature passed all the diagnostic tests presented in the Data Validation reports. The difference image centroiding test located the host star within $3\rlap{.}''18 \pm 2\rlap{.}''58$ of the source of the transit signal.

The light curves used in the analysis of each system are summarized in Table 2. For TOI 762 A we make use of the 2 min cadence TESS light curves corrected for systematics by SPOC using the Presearch

Data Conditioning Simple Aperture Photometry (PDC-SAP) method of Stumpe et al. (2012, 2014) and Smith et al. (2012). For TIC 46432937 we use the TESS-SPOC 30 min and 10 min cadence light curves, which were also corrected using the PDCSAP method. All of the *TESS* light curves were obtained from the Mikulski Archive for Space Telescopes (MAST) at the Space Telescope Science Institute (STScI).

### 2.2. *High Contrast Imaging*

TOI 762 A was observed with the Zorro speckle imager on the Gemini-South 8 m telescope (Scott et al. 2021). Observations were obtained in the $832 \pm 40$ nm and $562 \pm 54$ nm band-passes on 2020 Jan 11, and these were processed to generate reconstructed images following Howell et al. (2011). No companions to TOI 762 A were resolved through these observations within the field of view of Zorro, with contrast limits of $\Delta m_{832} > 5.42$ and $\Delta m_{562} > 4.9$ beyond $0\rlap{.}''5$. Figure 1 shows the 832 nm reconstructed image, and the resulting $5\sigma$ magnitude contrast limits that we place on any companions to TOI 762 A.

**Table 1**. Sources within $10''$ of TOI 762 A

| Parameter | TOI 762 A | TOI 762 B | |
|---|---|---|---|
| GAIA DR3 ID | 5362352744504000256 | 5362352744496315264 | 5362352744496318336 |
| $\Delta$R.A. (arcsec) | $\cdots$ | $-2.754 \pm 0.098$ | $5.501 \pm 0.092$ |
| $\Delta$Dec. (arcsec) | $\cdots$ | $-1.62 \pm 0.10$ | $4.003 \pm 0.092$ |
| $\mu_{\text{R.A.}}$ (mas yr$^{-1}$) | $-159.174 \pm 0.020$ | $-157.37 \pm 0.13$ | $-5.15 \pm 0.12$ |
| $\mu_{\text{Dec.}}$ (mas yr$^{-1}$) | $-24.780 \pm 0.020$ | $-24.38 \pm 0.12$ | $1.02 \pm 0.11$ |
| $\pi$ (mas) | $10.118 \pm 0.023$ | $9.79 \pm 0.14$ | $0.40 \pm 0.13$ |
| $G$ (mag) | $14.9297 \pm 0.0028$ | $18.1928 \pm 0.0031$ | $18.3444 \pm 0.0030$ |
| $BP - RP$ (mag)[a] | $2.7548 \pm 0.0059$ | $3.554 \pm 0.093$ | $0.994 \pm 0.020$ |
| $M_\star$ ($M_\odot$) | $0.442 \pm 0.025$ | $0.227 \pm 0.010$ | $\cdots$ |

[a] We caution that the $BP$ and $RP$ photometry for each source appears to be contaminated by the other neighboring sources as indicated by the high values of phot_bp_rp_excess_factor.

There are two resolved sources within $10''$ of TOI 762 A that are listed in the *Gaia* DR3 catalog (see also Table 1). Gaia DR3 5362352744496318336 is located $4\rlap{.}''7$ to the northeast from TOI 762 A with $\Delta G = 3.42$ mag, $\Delta BP = 2.29$ mag, and $\Delta RP = 4.05$ mag relative to TOI 762 A. The parallax and proper motion of this object differ significantly from the values for TOI 762 A indicating that the two sources are not physically associated. Gaia DR3 5362352744496315264 is located $3\rlap{.}''2$ to the southwest of TOI 762 A and does appear to be physically bound to TOI 762 A with $\pi = 9.79 \pm 0.14$ mas, pmRA $= -157.37 \pm 0.13$ mas yr$^{-1}$ and pmDE $= -24.38 \pm 0.12$ mas yr$^{-1}$ compared to $\pi =$

$10.118 \pm 0.023$ mas, pmRA $= -159.174 \pm 0.020$ mas yr$^{-1}$ and pmDE $= -24.780 \pm 0.020$ mas yr$^{-1}$ for TOI 762 A.

Gaia DR3 5362352744496315264 has $\Delta G = 3.26$ mag, $\Delta BP = 3.73$ mag and $\Delta RP = 2.93$ mag relative to TOI 762 A. This object has been identified as a wide binary companion to TOI 762 A in both the SUPERWIDE catalog (Hartman & Lépine 2020) and the catalog of El-Badry et al. (2021). We refer to this star as TOI 762 B. Assuming this is a bound companion, we estimate that it is a late-M dwarf star with a mass of $0.227 \pm 0.010\ M_\odot$, at a projected physical separation of $\sim 319$ AU from TOI 762 A. The mass estimate is based on comparing the absolute $G$ magnitude of the source to version 1.2

of the MIST theoretical stellar evolution models (Paxton et al. 2011, 2013, 2015; Choi et al. 2016; Dotter 2016), assuming the age, distance, metallicity and redenning to the source are the same as for TOI 762 A. The inferred 2MASS and WISE magnitudes for the star are $J = 14.057 \pm 0.086\,\mathrm{mag}$, $H = 13.475 \pm 0.076\,\mathrm{mag}$, $K_S = 13.177 \pm 0.085\,\mathrm{mag}$, $W_1 = 12.954 \pm 0.095\,\mathrm{mag}$, $W_2 = 12.71 \pm 0.10\,\mathrm{mag}$, $W_3 = 12.45 \pm 0.11\,\mathrm{mag}$, and $W_4 = 12.33 \pm 0.11\,\mathrm{mag}$. The measured relative proper motion difference between TOI 762 A and TOI 762 B of $\Delta\mathrm{pm} = 1.85 \pm 0.13\,\mathrm{mas\,yr}^{-1}$ is less than the value of $2.9\,\mathrm{mas\,yr}^{-1}$ that would be expected if the binary star system has a circular, face-on orbit, and suggests that the orbit is inclined and/or eccentric. We note that TOI 762 B is resolved from TOI 762 A in the spectroscopic observations (Section 2.4) which reveal a RV variation for TOI 762 A that is in phase with the transit ephemeris. Based on this we conclude that TOI 762 A is the source of the transit signal.

The closer of the two neighbors is within the photometric aperture of the follow-up light curves for TOI 762 A, and would also have been unresolved in the 2MASS and WISE photometry of this source. The source is also close enough to be of concern for the *Gaia BP* and *RP* measurements. Using the relations in Riello et al. (2021) for the expected value and scatter of phot_bp_rp_excess_factor as functions of the $BP - RP$ color and $G$ magnitude for an isolated source, we find that TOI 762 A has a value that is $3.3\sigma$ greater than expected. This indicates that these measurements may be contaminated, however correcting for this contamination may be difficult to do accurately. For this reason we exclude the $BP$ and $RP$ photometry from the analysis of this system. We account for the contamination in the follow-up light curves as described in Section 3.3. To account for the contamination in the 2MASS and WISE photometry we use MIST v 1.2 to estimate the apparent magnitude of the neighbor in these band-passes given the absolute $G$ magnitude, and assuming the age, metallicity, distance, and redenning to the source have the values that we determine for TOI 762 A. We then subtract the flux contribution of the neighbor from the observed 2MASS and WISE magnitudes, accounting for the uncertainty on the flux of the neighbor. These corrected magnitudes are listed in Table 4, and are also the values that we include in our analysis of the system (Section 3.3).

There are no nearby stars within $10''$ of TIC 46432937 listed in the *Gaia* DR3 catalog. Ground-based high-spatial-resolution imaging is not available for this target, so stellar companions within $1''$ cannot be ruled out.
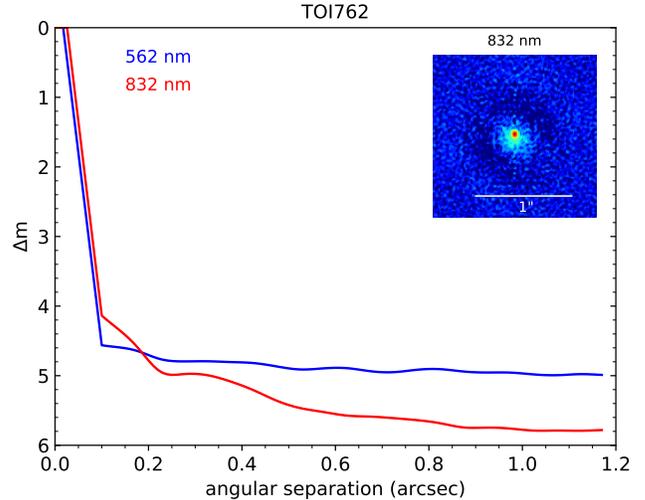


**Figure 1.** $5\sigma$ magnitude contrast limits for any companions to TOI 762 A based on Gemini/Zorro observations obtained in the 562 nm and 832 nm band-passes. The inset shows the reconstructed Gemini/Zorro image of TOI 762 A in the 832 nm band-pass.

### 2.3. *Ground-based Photometric Follow-up*

Ground-based photometric follow-up observations of TOI 762 A were obtained through the *TESS* Follow-up Program (TFOP; Collins 2019). Photometric follow-up observations of TIC 46432937 were also obtained. The observations that have been carried out for these systems are listed in Table 2. The data are shown in Figures 2 and 5, and are made available in Table 3. Here we briefly discuss each facility that was used.

#### 2.3.1. *LCOGT 1 m*

A transit of TOI 762 A b was observed using a 1 m telescope at the Siding Spring Observatory, Australia station of the Las Cumbres Observatory Global Telescope (LCOGT) network (Brown et al. 2013). The observations were gathered through an $I_C$ band-pass on 2019 June 28 using a SINISTRO imager. The images have a pixel scale of $0\farcs389\,\mathrm{px}^{-1}$, with an estimated average point-spread function (PSF) full-width at half-maximum (FWHM) of $\sim 2''$. The data were reduced to ensemble-corrected light curves using the AstroImageJ package (Collins et al. 2017) with a photomeric aperture radius of 14 pixels.

A separate photometric measurement was performed on the LCOGT images using a 2 pixel ($0\farcs8$) radius aperture to confirm that the transits are due to TOI 762 A rather than the neighbor TOI 762 B. This analysis revealed that TOI 762 A is indeed the source of the $\sim 30\,\mathrm{ppt}$ transit events.

#### 2.3.2. *ExTrA 0.6 m*

A total of six transits of TOI 762 A b and six transits of TIC 46432937 b were monitored using the Exoplanets in Transits and their Atmospheres (ExTrA) facility (Bonfils et al. 2015) at La Silla Observatory in Chile. Several of the transits were simultaneously observed by more than one of the three 0.6 m telescopes in the facility, and for TIC 46432937 b we made multi-band light curves from the observations, leading to a total of 14 separate transit light curves of TOI 762 A b and 64 separate light curves of TIC 46432937 b from this facility. The facility performs spectro-photometric observations over a wavelength range of $0.85\,\mu m$ to $1.55\,\mu m$ using a NIRvana 640 LN camera which is fed with optical fibers from the three telescopes. Observations of TOI 762 A were gathered with the $4''$ diameter aperture fibers, except for on the night of 2021 Mar 13 when the $8''$ fibers were used. All transits of TIC 46432937 were observed with $8''$ diameter aperture fibers. Both targets were observed with the low resolution mode of the spectrograph ($R \sim 20$). Band-pass-integrated, comparison-star-corrected light curves were produced following the method of Cointepas et al. (2021). For TOI 762 A we made use of light curves integrated over the full band-pass of the instrument, while for TIC 46432937, where the grazing transits make the solution more sensitive to limb darkening, we produced and analyzed separate $Z$, $Y$, $J$ and $H$-band light curves from each transit observation.

### 2.3.3. *TRAPPIST-South 0.6 m*

Two transits of TOI 762 A b were observed using the southern 0.6 m TRAnsiting Planets and PlanetesImals Small Telescope (TRAPPIST-South; Jehin et al. 2011; Gillon et al. 2011; Barkaoui et al. 2019) at La Silla Observatory. The first transit on 2023 February 2 was observed through an $I + z$ filter, while the second transit on 2023 April 16 was observed through a $z'$ filter. Observations were obtained at a pixel scale of $0''.64$. For the first transit the estimated PSF FWHM was $2''.6$ and a photometric aperture of $3''.84$ was used, while for the second transit the estimated PSF FWHM was $1''.4$ and a photometric aperture of $4''.48$ was used. Scheduling of the observations was performed using the tools of Jensen (2013), while ensemble-corrected light curves were derived from the observations following the methods of Garcia et al. (2022).

### 2.3.4. *SPECULOOS-South 1.0 m*

A transit of TOI 762 A b was observed on 2023 April 16 using three of the 1.0 m telescopes in the Search for habitable Planets EClipsing ULtra-cOOl Stars Southern observatory (SPECULOOS-South Delrez et al. 2018; Sebastian et al. 2021; Burdanov et al. 2022) at Paranal Observatory in Chile. Observations were gathered through $g'$, $r'$ and $z'$ filters. The observations had a pixel scale of $0''.35$ and an estimated PSF FWHM of $1''.6$. An aperture of radius $2''.45$ was used to extract the photometry. Scheduling of the observations was performed following Sebastian et al. (2021), while the data were reduced to ensemble-corrected light curves following Murray et al. (2020) and Garcia et al. (2021, 2022).

### 2.4. *Spectroscopic Observations*

Time series spectroscopy was obtained for both TOI 762 A and TIC 46432937 using the ESPRESSO instrument (Pepe et al. 2021) on the 8 m Very Large Telescope (VLT) at Paranal Observatory in Chile. We obtained five observations of TOI 762 A in Period 104 between 2019 Dec 1 and 2019 Dec 24, and three observations in Period 110 between 2022 Dec 25 and 2022 Dec 30. We allow for an instrumental offset between the two periods in fitting the observations of TOI 762 A. For TIC 46432937, we obtained eight observations all in Period 110, between 2022 Nov 24 and 2023 Feb 22. Observations were gathered in HR mode (using a single Unit Telescope, and a spectroscopic resolution of $R \equiv \Delta\lambda/\lambda \sim 140,000$; the fiber aperture is $1''$ in this mode, and the wavelength coverage is from $3770\,\text{Å}$ to $7910\,\text{Å}$). A sky fiber was placed $7''$ from the target fiber, however there is no difference in the RVs derived from the sky-subtracted spectra compared to the non-sky-subtracted spectra due to the fact that moon contamination was minimal during the observations. An exposure time of 1800 s was used for the observations. For TOI 762 A the peak S/N varied from 23 to 30, while for TIC 46432937 the peak S/N was between 41 and 64.

The data were reduced to Radial Velocity (RV) measurements in the Solar System Barycentric frame using the ESPRESSO DRS pipeline (v2.3.5 Sosnowska et al. 2015; Modigliani et al. 2020) in the EsoReflex environment (Freudling et al. 2013). The ESPRESSO DRS calculates the RVs from individual spectra by measuring the cross correlation function (CCF) for each slice separately, using a template (stellar model) matching closest to the spectral type of the star. It then adds all these CCFs for the different orders, ignoring those orders that are severely affected by telluric contamination. It then fits a Gaussian function to the final CCF, where the center of the Gaussian is the RV and the width of the Gaussian represents the precision of the RV measurements.

Both systems show significant RV variations that are in phase with the transit ephemerides, and of amplitudes that indicate the transiting components are of planetary mass in both cases. The RV measurements for each

system are shown in Figures 2 and 4 and are listed in Table 5.

**Table 2**. Summary of photometric observations

| Instrument/Field[a] | Date(s) | # Images[b] | Cadence[c] (sec) | Filter | Precision[d] (mmag) |
|---|---|---|---|---|---|
| **TOI 762 A** | | | | | |
| TESS/Sector 10 | 2019 Mar–2019 Apr | 13,754 | 120 | $T$ | 11.7 |
| TESS/Sector 36 | 2021 Mar–2021 Apr | 15,491 | 120 | $T$ | 13.3 |
| TESS/Sector 37 | 2021 Apr | 15,061 | 120 | $T$ | 13.9 |
| TESS/Sector 63 | 2023 Mar–2023 Apr | 17,456 | 120 | $T$ | 12.5 |
| LCOGT 1.0 m | 2019 Jun 28 | 109 | 97 | $I_C$ | 3.1 |
| ExTrA - tel2 | 2021 Mar 13 | 214 | 62 | 0.85–1.55 $\mu$m | 5.9 |
| ExTrA - tel2 | 2021 Mar 27 | 168 | 62 | 0.85–1.55 $\mu$m | 4.7 |
| ExTrA - tel3 | 2021 Mar 27 | 164 | 62 | 0.85–1.55 $\mu$m | 5.5 |
| ExTrA - tel2 | 2021 Apr 24 | 159 | 62 | 0.85–1.55 $\mu$m | 5.7 |
| ExTrA - tel3 | 2021 Apr 24 | 160 | 62 | 0.85–1.55 $\mu$m | 7.5 |
| TRAPPIST-South | 2023 Feb 2 | 214 | 83 | I+$z$ | 3.5 |
| ExTrA - tel1 | 2023 Apr 9 | 129 | 62 | 0.85–1.55 $\mu$m | 7.3 |
| ExTrA - tel2 | 2023 Apr 9 | 131 | 62 | 0.85–1.55 $\mu$m | 4.8 |
| ExTrA - tel3 | 2023 Apr 9 | 131 | 62 | 0.85–1.55 $\mu$m | 5.0 |
| SPECULOOS-South | 2023 Apr 16 | 97 | 210 | $g'$ | 3.2 |
| SPECULOOS-South | 2023 Apr 16 | 169 | 85 | $r'$ | 3.2 |
| SPECULOOS-South | 2023 Apr 16 | 565 | 36 | $z'$ | 2.9 |
| ExTrA - tel1 | 2023 Apr 16 | 162 | 62 | 0.85–1.55 $\mu$m | 7.4 |
| ExTrA - tel2 | 2023 Apr 16 | 167 | 62 | 0.85–1.55 $\mu$m | 4.4 |
| ExTrA - tel3 | 2023 Apr 16 | 169 | 62 | 0.85–1.55 $\mu$m | 5.4 |
| TRAPPIST-South | 2023 Apr 16 | 141 | 111 | $z'$ | 3.0 |
| ExTrA - tel1 | 2023 Apr 23 | 173 | 62 | 0.85–1.55 $\mu$m | 11.2 |
| ExTrA - tel2 | 2023 Apr 23 | 175 | 62 | 0.85–1.55 $\mu$m | 6.1 |
| ExTrA - tel3 | 2023 Apr 23 | 174 | 62 | 0.85–1.55 $\mu$m | 8.7 |
| **TIC 46432937** | | | | | |
| TESS/Sector 6 | 2018 Dec – 2019 Jan | 959 | 1800 | $T$ | 1.2 |
| TESS/Sector 32 | 2020 Nov – 2020 Dec | 3467 | 600 | $T$ | 2.4 |
| ExTrA - tel1 | 2023 Oct 10 | 141 | 62 | $Z$ | 7.7 |
| ExTrA - tel1 | 2023 Oct 10 | 141 | 62 | $Y$ | 4.7 |
| ExTrA - tel1 | 2023 Oct 10 | 140 | 62 | $J$ | 4.3 |
| ExTrA - tel1 | 2023 Oct 10 | 141 | 62 | $H$ | 12.6 |
| ExTrA - tel2 | 2023 Oct 10 | 140 | 62 | $Z$ | 7.0 |
| ExTrA - tel2 | 2023 Oct 10 | 140 | 62 | $Y$ | 5.0 |
| ExTrA - tel2 | 2023 Oct 10 | 140 | 62 | $J$ | 4.3 |
| ExTrA - tel2 | 2023 Oct 10 | 141 | 62 | $H$ | 12.6 |
| ExTrA - tel3 | 2023 Oct 10 | 141 | 62 | $Z$ | 7.1 |
| ExTrA - tel3 | 2023 Oct 10 | 141 | 62 | $Y$ | 5.9 |
| ExTrA - tel3 | 2023 Oct 10 | 141 | 62 | $J$ | 5.3 |
| ExTrA - tel3 | 2023 Oct 10 | 140 | 62 | $H$ | 22.8 |
| ExTrA - tel1 | 2023 Nov 5 | 165 | 62 | $Z$ | 9.9 |
| ExTrA - tel1 | 2023 Nov 5 | 165 | 62 | $Y$ | 5.6 |

*Table 2 continued*

Hartman et al.

**Table 2** *(continued)*

| Instrument/Field[a] | Date(s) | # Images[b] | Cadence[c] (sec) | Filter | Precision[d] (mmag) |
|---|---|---|---|---|---|
| ExTrA - tel1 | 2023 Nov 5 | 165 | 62 | J | 5.2 |
| ExTrA - tel1 | 2023 Nov 5 | 163 | 62 | H | 14.7 |
| ExTrA - tel2 | 2023 Nov 5 | 163 | 62 | Z | 7.5 |
| ExTrA - tel2 | 2023 Nov 5 | 165 | 62 | Y | 5.4 |
| ExTrA - tel2 | 2023 Nov 5 | 165 | 62 | J | 5.3 |
| ExTrA - tel2 | 2023 Nov 5 | 165 | 62 | H | 14.7 |
| ExTrA - tel3 | 2023 Nov 5 | 165 | 62 | Z | 8.9 |
| ExTrA - tel3 | 2023 Nov 5 | 165 | 62 | Y | 5.7 |
| ExTrA - tel3 | 2023 Nov 5 | 164 | 62 | J | 6.0 |
| ExTrA - tel3 | 2023 Nov 5 | 165 | 62 | H | 18.8 |
| ExTrA - tel1 | 2023 Nov 18 | 269 | 62 | Z | 8.0 |
| ExTrA - tel1 | 2023 Nov 18 | 268 | 62 | Y | 4.9 |
| ExTrA - tel1 | 2023 Nov 18 | 269 | 62 | J | 4.6 |
| ExTrA - tel1 | 2023 Nov 18 | 270 | 62 | H | 12.2 |
| ExTrA - tel2 | 2023 Nov 18 | 269 | 62 | Z | 7.6 |
| ExTrA - tel2 | 2023 Nov 18 | 269 | 62 | Y | 4.8 |
| ExTrA - tel2 | 2023 Nov 18 | 268 | 62 | J | 4.5 |
| ExTrA - tel2 | 2023 Nov 18 | 270 | 62 | H | 11.8 |
| ExTrA - tel3 | 2023 Nov 18 | 269 | 62 | Z | 8.6 |
| ExTrA - tel3 | 2023 Nov 18 | 268 | 62 | Y | 4.9 |
| ExTrA - tel3 | 2023 Nov 18 | 269 | 62 | J | 5.2 |
| ExTrA - tel3 | 2023 Nov 18 | 269 | 62 | H | 14.8 |
| ExTrA - tel1 | 2023 Dec 1 | 221 | 62 | Z | 8.1 |
| ExTrA - tel1 | 2023 Dec 1 | 221 | 62 | Y | 5.8 |
| ExTrA - tel1 | 2023 Dec 1 | 220 | 62 | J | 5.0 |
| ExTrA - tel1 | 2023 Dec 1 | 220 | 62 | H | 11.8 |
| ExTrA - tel2 | 2023 Dec 1 | 219 | 62 | Z | 8.0 |
| ExTrA - tel2 | 2023 Dec 1 | 219 | 62 | Y | 5.6 |
| ExTrA - tel2 | 2023 Dec 1 | 220 | 62 | J | 4.7 |
| ExTrA - tel2 | 2023 Dec 1 | 220 | 62 | H | 15.1 |
| ExTrA - tel3 | 2023 Dec 1 | 220 | 62 | Z | 9.0 |
| ExTrA - tel3 | 2023 Dec 1 | 220 | 62 | Y | 5.9 |
| ExTrA - tel3 | 2023 Dec 1 | 220 | 62 | J | 5.9 |
| ExTrA - tel3 | 2023 Dec 1 | 221 | 62 | H | 16.4 |
| ExTrA - tel1 | 2023 Dec 14 | 312 | 62 | Z | 8.3 |
| ExTrA - tel1 | 2023 Dec 14 | 313 | 62 | Y | 5.3 |
| ExTrA - tel1 | 2023 Dec 14 | 314 | 62 | J | 4.8 |
| ExTrA - tel1 | 2023 Dec 14 | 313 | 62 | H | 15.8 |
| ExTrA - tel3 | 2023 Dec 14 | 314 | 62 | Z | 8.2 |
| ExTrA - tel3 | 2023 Dec 14 | 314 | 62 | Y | 5.6 |
| ExTrA - tel3 | 2023 Dec 14 | 311 | 62 | J | 5.8 |
| ExTrA - tel3 | 2023 Dec 14 | 313 | 62 | H | 15.9 |
| ExTrA - tel1 | 2024 Jan 6 | 141 | 62 | Z | 8.6 |
| ExTrA - tel1 | 2024 Jan 6 | 141 | 62 | Y | 5.2 |
| ExTrA - tel1 | 2024 Jan 6 | 141 | 62 | J | 5.0 |
| ExTrA - tel1 | 2024 Jan 6 | 140 | 62 | H | 12.7 |
| ExTrA - tel3 | 2024 Jan 6 | 141 | 62 | Z | 8.7 |
| ExTrA - tel3 | 2024 Jan 6 | 140 | 62 | Y | 5.7 |
| ExTrA - tel3 | 2024 Jan 6 | 141 | 62 | J | 6.2 |

*Table 2 continued*

**Table 2** *(continued)*

| Instrument/Field[a] | Date(s) | # Images[b] | Cadence[c] (sec) | Filter | Precision[d] (mmag) |
|---|---|---|---|---|---|
| ExTrA - tel3 | 2024 Jan 6 | 140 | 62 | *H* | 16.4 |

[a] For *TESS* data we list the Sector from which the observations are taken.

[b] Excluding any outliers or other data not included in the modelling.

[c] The median time between consecutive images rounded to the nearest second. Due to factors such as weather, the day–night cycle, guiding and focus corrections the cadence is only approximately uniform over short timescales.

[d] The RMS of the residuals from the best-fit model. Note that in the case of *TESS* observations the transit may appear artificially shallower due to over-filtering and/or blending from unresolved neighbors. As a result the S/N of the transit may be less than what would be calculated from $R_p/R_\star$ and the RMS estimates given here.

**Table 3.** Light curve data for TOI 762 A and TIC 46432937.

| Object[a] | BJD[b] | Mag[c] | $\sigma_{\mathrm{Mag}}$ | Mag(orig)[d] | Filter | Instrument |
|---|---|---|---|---|---|---|
| TOI-762 | 2458595.24514 | 0.01246 | 0.01259 | $\cdots$ | $T$ | TESS/Sec10 |
| TOI-762 | 2458577.88699 | $-0.00409$ | 0.01237 | $\cdots$ | $T$ | TESS/Sec10 |
| TOI-762 | 2458588.30220 | $-0.01125$ | 0.01251 | $\cdots$ | $T$ | TESS/Sec10 |
| TOI-762 | 2458581.35921 | $-0.01476$ | 0.01231 | $\cdots$ | $T$ | TESS/Sec10 |
| TOI-762 | 2458591.77437 | $-0.02359$ | 0.01222 | $\cdots$ | $T$ | TESS/Sec10 |
| TOI-762 | 2458574.41615 | 0.01873 | 0.01261 | $\cdots$ | $T$ | TESS/Sec10 |
| TOI-762 | 2458595.24653 | $-0.01866$ | 0.01228 | $\cdots$ | $T$ | TESS/Sec10 |
| TOI-762 | 2458577.88838 | $-0.01855$ | 0.01225 | $\cdots$ | $T$ | TESS/Sec10 |
| TOI-762 | 2458588.30358 | $-0.00049$ | 0.01260 | $\cdots$ | $T$ | TESS/Sec10 |
| TOI-762 | 2458581.36059 | $-0.01694$ | 0.01228 | $\cdots$ | $T$ | TESS/Sec10 |

[a] Either TOI 762 A or TIC 46432937.

[b] Barycentric Julian Dates in this paper are reported on the Barycentric Dynamical Time (TDB) system.

[c] The out-of-transit level has been subtracted. For observations made with TESS these magnitudes have been corrected for trends *prior* to fitting the transit model. For observations made with follow-up instruments (anything other than "TESS" in the "Instrument" column), the magnitudes have been corrected for a quadratic trend in time fit simultaneously with the transit.

[d] Raw magnitude values without correction for the quadratic trend in time, or for trends correlated with the seeing. These are only reported for the follow-up observations.

NOTE— This table is available in a machine-readable form in the online journal. A portion is shown here for guidance regarding its form and content.

**TOI-762  P=3.47d  M$_P$=0.25M$_{Jup}$  R$_P$=0.74R$_{Jup}$  M$_S$=0.44M$_{Sun}$  R$_S$=0.42R$_{Sun}$**
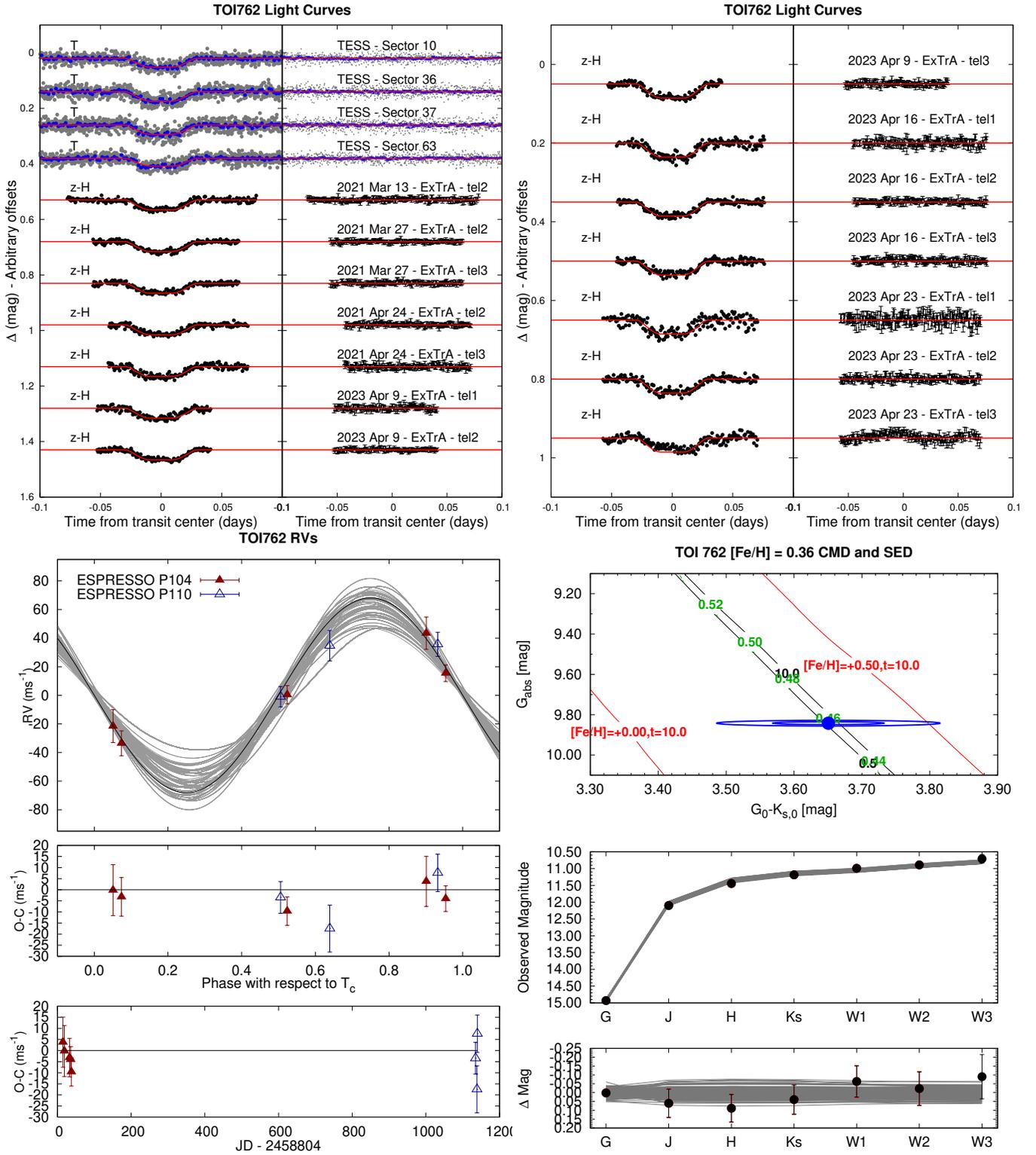


**Figure 2.** Observations incorporated into the analysis of the transiting planet system TOI 762 A. Additional light curves are shown in Fig. 3. *Top:* Transit light curves with best-fitted model (maximum likelihood) overplotted. The dates, filters and instruments used are indicated. The term $z - H$ used for the ExTrA light curves refers to the full band-pass not the color. (Caption continued on next page.)

**Figure 2.** (Caption continued from previous page.) For *TESS* we phase-fold the data, and plot the un-binned observations in grey, with the phase-binned values overplotted in blue. The residuals for each light curve are shown on the right-hand-side in the same order as the original light curves. The error bars represent the photon and background shot noise, plus the readout noise. Note that these uncertainties are scaled in the fitting procedure to achieve a reduced $\chi^2$ of unity, but the uncertainties shown in the plot have not been scaled. *Bottom Left:* High-precision RVs phased with respect to the mid-transit time. The top panel shows the phased measurements together with the best-fit (maximum likelihood) model with no eccentricity. The gray-scale curves show 1000 models randomly selected from the MCMC posterior distribution generated when the eccentricity is allowed to vary. The center-of-mass velocity has been subtracted. The middle panel shows the phase-folded velocity $O-C$ residuals. The error bars include the estimated jitter, which is varied as a free parameter in the fitting. The bottom panel shows the $O-C$ residuals as a function of time. *Bottom Right:* Color-magnitude diagram (CMD) and spectral energy distribution (SED). The top panel shows the absolute $G$ magnitude vs. the de-reddened $G - K_S$ color compared to theoretical isochrones (black lines) and stellar evolution tracks (green lines) from the MIST models interpolated at the best-estimate value for the metallicity of the host. The age of each isochrone is listed in black in Gyr, while the mass of each evolution track is listed in green in solar masses. The solid red lines show isochrones at higher and lower metallicities than the best-estimate value, with the metallicity and age in Gyr of each isochrone labelled on the plot. The filled blue circles show the measured reddening- and distance-corrected values from *Gaia* DR3 and 2MASS, while the blue lines indicate the $1\sigma$ and $2\sigma$ confidence regions, including the estimated systematic errors in the photometry. The middle panel shows the SED as measured via broadband photometry through the listed filters. Here we plot the observed magnitudes without correcting for distance or extinction. Overplotted are 200 model SEDs randomly selected from the MCMC posterior distribution produced through the global analysis (gray lines). The model makes use of the predicted absolute magnitudes in each bandpass from the MIST isochrones, the distance to the system (constrained largely via *Gaia* DR3) and extinction (constrained from the SED with a prior coming from the MWDUST 3D Galactic extinction model). The bottom panel shows the $O-C$ residuals from the best-fit model SED. The errors listed in the catalogs for the broad-band photometry measurements are shown with black lines, while the errors including an assumed 0.02 mag systematic uncertainty, which is added in quadrature to the listed uncertainties, are shown with red lines. These latter uncertainties are what we use in the fit.
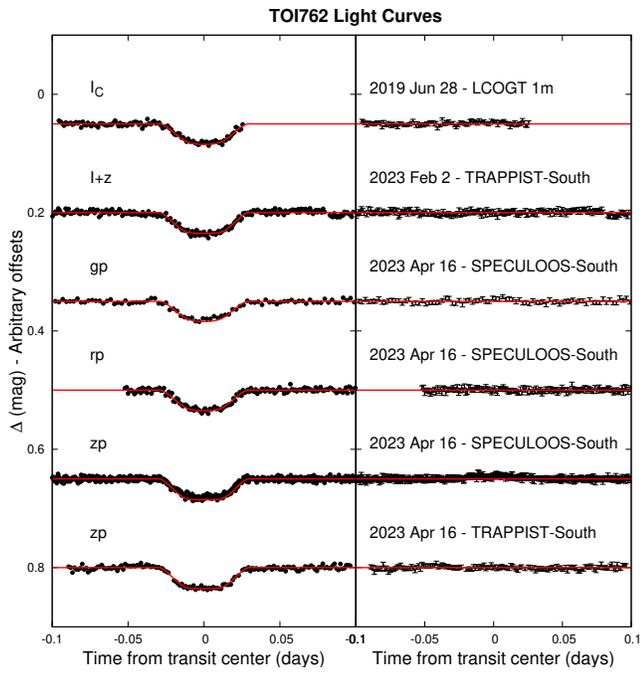
**Figure 3.** Additional follow-up light curves of TOI 762 A, shown as described in Fig. 2.

# TIC-46432937  P=1.44d  M$_P$=3.20M$_{Jup}$  R$_P$=1.19R$_{Jup}$  M$_S$=0.56M$_{Sun}$  R$_S$=0.53R$_{Sun}$
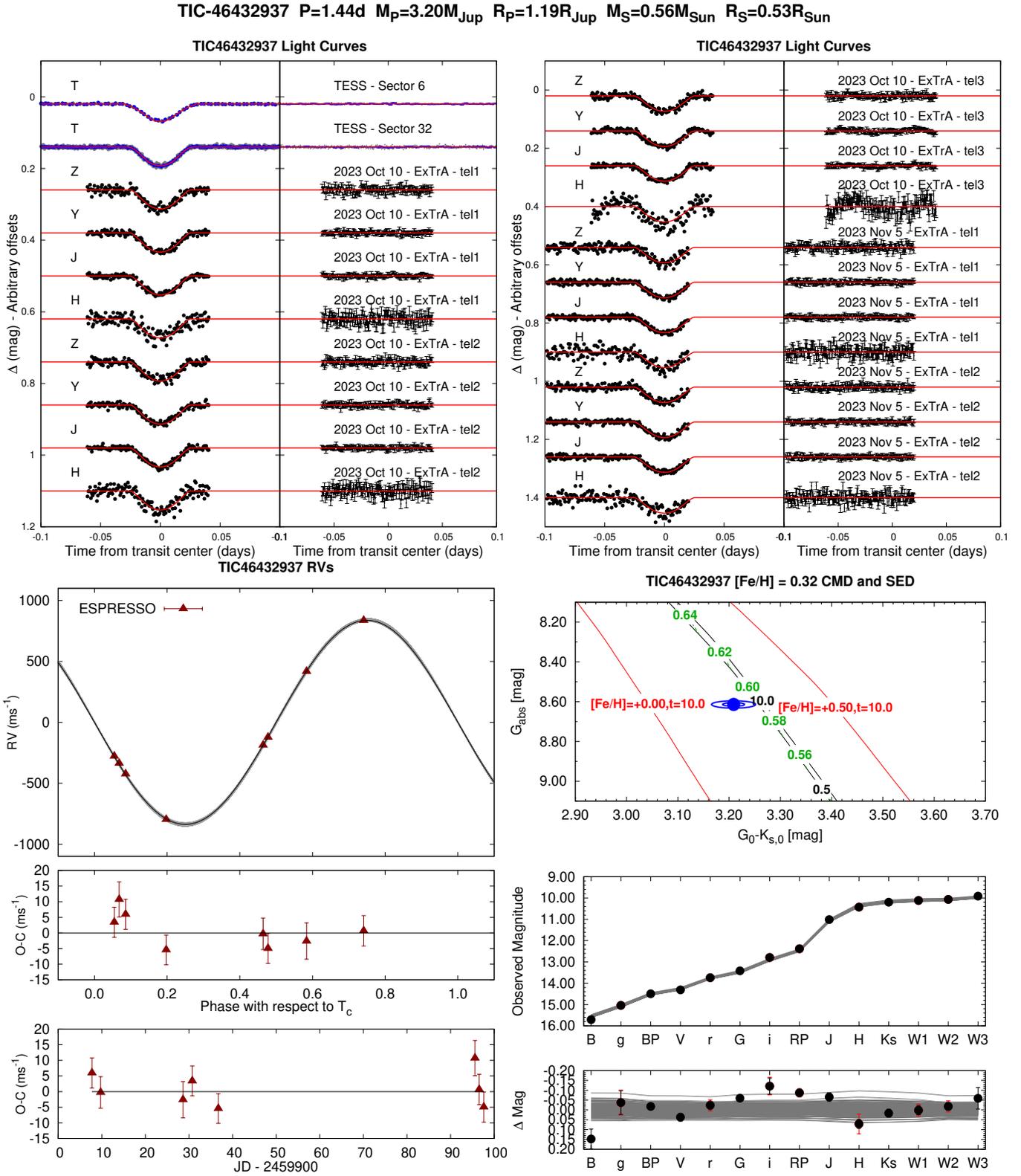


**Figure 4.** Same as Figure 2, here we show the observations of TIC 46432937 together with our best-fit model. Additional follow-up light curves of TIC 46432937 are shown in Figure 5.
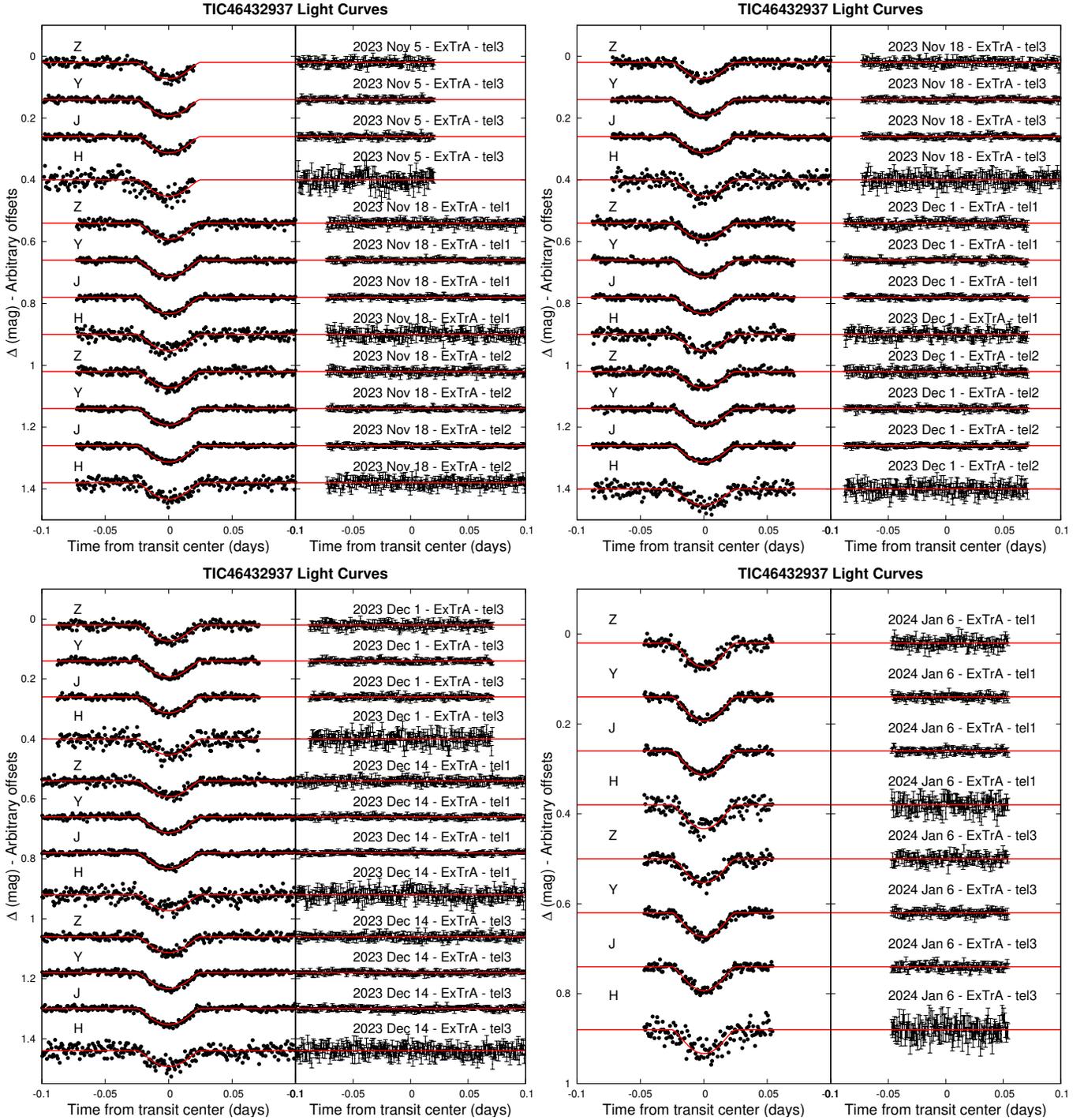
**Figure 5.** Additional follow-up light curves of TIC 46432937, shown as described in Fig. 2.

## 3. ANALYSIS

### 3.1. Derivation of Stellar Atmospheric Parameters

We used the machine-learning based ODUSSEAS package (Antoniadis-Karnavas et al. 2020) to measure the photospheric effective temperature $T_{\mathrm{eff}\star}$ and metallicity [Fe/H] (assuming Solar-scaled abundances) of both systems from the ESPRESSO spectra. The tool measures pseudo-equivalent widths for thousands of lines and compares them to a training set of reference M dwarf stars observed by HARPS. Although the HARPS spectra have lower resolution than the ESPRESSO spectra, the tools has been shown to work effectively on high resolution ESPRESSO spectra as well (Lillo-Box et al. 2020). The analysis was performed using the "wide error" mode, taking into consideration the intrinsic uncertainties of the reference parameters in the machine learning process in addition to the output machine learning model errors. We measure $T_{\mathrm{eff}\star} = 3150 \pm 67\,\mathrm{K}$ and [Fe/H] $= 0.24 \pm 0.10$ for TOI 762 A and $T_{\mathrm{eff}\star} = 3535 \pm 65\,\mathrm{K}$ and [Fe/H] $= 0.03 \pm 0.10$ for TIC 46432937.

### 3.2. Stellar Activity and Galactic Kinematics

We checked the *TESS* light curves of TOI 762 A for evidence of stellar rotational variability or flaring events. No significant out-of-transit variability is observed. A total of 6 bright outliers ($> 5\sigma$) are present in the out-of-transit *TESS* light curves of TOI 762 A. In each case the outlier is isolated to a single point, so if it is due to a flare, the flare would have been shorter than 120 s in duration. It is worth noting though that no $5\sigma$ faint outliers are detected. We also checked the publicly available ASAS-SN (Hart et al. 2023; Shappee et al. 2014) light curve TOI 762 A and see no evidence for periodic variability or stellar flares.

For TIC 46432937 a periodic signal is present in the out-of-transit *TESS* light curves from Sectors 6 and 32. We find a period of $P = 5.88 \pm 0.54\,\mathrm{day}$ with a signal-to-noise ratio of 35.2 as measured in the Generalized Lomb-Scargle periodogram (Zechmeister & Kürster 2009). The estimated uncertainty on the period is the half-width at half-maximum of the peak in the periodogram. The peak-to-peak variation in the phase-binned light curve is $\sim 1\,\mathrm{mmag}$. The formal false alarm probability is vanishingly small, however this does not account for the possibility of systematic variations in the light curve due to uncorrected instrumental effects. We checked the Zwicky Transient Facility (ZTF; Masci et al. 2019) DR20 light curve of TIC 46432937, but see no evidence for periodic variability. However, the scatter in the ZTF light curve of this source is $\sim 0.02\,\mathrm{mag}$, and the $\sim 1\,\mathrm{mmag}$ amplitude signal seen in *TESS* would not be detectable if it is present in the ZTF data. No variability is detected in the publicly available ASAS-SN light curve of TIC 46432937 either, which also has too high a scatter to permit detection of a signal comparable to that seen in the *TESS* data. No candidate flare events or significant bright outliers are seen in the *TESS* light curve of TIC 46432937. While bright outliers are seen in the ZTF and ASAS-SN light curves, the number of faint outliers is comparable.

If the $P = 5.88$ day signal corresponds to the rotation period of TIC 46432937, the rotation period would be faster than the bulk of early M dwarf stars with $0.9 < G - RP < 1.1$ seen in the *Kepler* sample (McQuillan et al. 2014). While this may suggest a young age for TIC 46432937, existing gyrochronology relations are not suitable for M dwarf stars (Popinchalk et al. 2021). It is also unclear how a relatively massive $\sim 3\,M_{\mathrm{J}}$ planet on a short $P = 1.44$ day orbit might affect the rotational evolution of an early M dwarf. For these reasons we do not attempt to estimate an age for TIC 46432937 based on the possible rotation period.

As an additional check on the ages of the systems, we used the systemic radial velocities that we measured for each star with ESPRESSO, together with the position, parallax, and proper motions from *Gaia* DR3 to compute the $U$, $V$, and $W$ space velocities. We follow the convention that $U$ increases toward the Galactic center, $V$ increases in the direction of Galactic rotation, and $W$ increases toward the North Galactic Pole. These velocities are then corrected to be relative to the local standard of rest (LSR) by adding the Solar peculiar velocities of $(U_{\odot}, V_{\odot}, W_{\odot}) = (11.10, 12.24, 7.25)\,\mathrm{km\,s^{-1}}$ from Schönrich et al. (2010). This yields $(U_{LSR}, V_{LSR}, W_{LSR}) = (-35.56, -58.28, -22.96)\,\mathrm{km\,s^{-1}}$ and $(-73.82, -33.11, -31.21)\,\mathrm{km\,s^{-1}}$, for TOI 762 A and TIC 46432937, respectively. We use these velocities to compute the relative probabilities of each star being a member of the Galactic thin and thick disks, or of the Galactic halo, following Bensby et al. (2014). We find that both objects have a 70% probability of being members of the thin disk, a 30% probability of being members of the thick disk, and negligible probabilities of being members of the Galactic halo. While each object is more likely than not to be in the thin disk, both stars exhibit fairly high space motion compared to typical thin disk members (both stars have at least one component of their space velocity that is different from the mean value for thin disk stars by more than $2\sigma$), which is consistent with both objects being older main sequence stars.

### 3.3. Joint Stellar and Planet Modeling

We carried out a joint analysis of the available observations to determine the stellar and planetary parameters of each system following the method of Hartman et al. (2019) and Bakos et al. (2020). For each object we performed a simultaneous fit to all light curves, RV measurements, the observed Spectral-Energy Distribution (SED) as traced by the available catalog broad-band photometry, the spectroscopic $T_{\mathrm{eff}\star}$ and [Fe/H], and the astrometric parallax from *Gaia* DR3 (Gaia Collaboration et al. 2022). The catalog photometry, spectroscopic parameters, and parallax values that we included in the fit for each system are listed in Table 4. The light curves were modeled using the semi-analytic Mandel & Agol (2002) model with quadratic limb darkening coefficients that were allowed to vary in the fit, but with priors based on the stellar atmospheric parameters in the theoretical tabulations by Claret et al. (2012, 2013); Claret (2018). For the *TESS* observations of TIC 46432937, which have exposure times of 30 min or 10 min, we integrated the model over the exposure time. The RVs were fit assuming the star follows a Keplerian orbit around the system barycenter. The stellar parameters and SED are constrained to follow the MIST stellar evolution model while allowing for systematic errors in the stellar physical parameters following the procedure of Hartman et al. (2023). We adopt systematic errors of 0.08 dex, 2.4%, 5% and 0.021 mag on the metallicity, effective temperature, stellar mass, and bolometric magnitudes in the stellar evolution models, respectively (Tayar et al. 2022). We impose a prior on the line of sight extinction $A_V$ using the MWDUST 3D Galactic extinction model (Bovy et al. 2016) and assume an $R_V = 3.1$ extinction law. The fit is performed twice for each system, first assuming a circular orbit for the planet, and second allowing for a non-zero eccentricity. The fit is carried out through a differential evolution Markov Chain Monte Carlo procedure (see Hartman et al. 2019 for a full list of parameters and priors) using visual inspection to confirm that the chains are converged and well-mixed, and to set the burn-in period.

To account for dilution in the light curves of TOI 762 A due to the neighboring star TOI 762 B, we include for each light curve a parameter that specifies the fraction of the flux in the light curve that comes from the transit hosting star when out of transit (with the remaining fraction assumed to come from a constant source). This parameter is allowed to vary in the fit independently for each light curve. We place a prior and uncertainty on each of these dilution parameters by calculating the expected flux from TOI 762 B that would contaminate the aperture, assuming that TOI 762 B has the same distance, reddening, age, and metallicity as inferred for

TOI 762 A, and using the $G$ magnitude together with the MIST isochrones to infer the mass of TOI 762 B and its expected magnitude in various passbands. We note that the resulting dilution values are all consistent with the priors, to within the uncertainties. No systematic trend with wavelength is observed in the residuals.

The observations are consistent with circular orbits for both systems. For TOI 762 A b we place a 95% confidence upper limit on the eccentricity of $e < 0.083$, while for TIC 46432937 b the upper limit is $e < 0.009$. We therefore adopt the parameters derived for each system assuming a circular orbit. Note that in the joint fitting that we perform, the constraints on the eccentricities of these systems come not just from the RVs, but also from the combination of the transit observations and the theoretical stellar evolution models that constrain the allowed combinations of stellar mass, radius, and metallicity. For M dwarf host stars the constraints on mass and radius from comparing the observations to stellar evolution models are much tighter than for higher mass stars, which can lead to a much tighter constraint on the eccentricity than might be allowed by the RVs alone (e.g., Hartman et al. 2015). This appears to be the case for TOI 762 A b, for which the RVs alone provide a much less stringent constraint on the eccentricity than is achieved through our joint analysis of the data. For TIC 46432937 b on the other hand, the eccentricity constraint appears to come primarily from the RVs. Here the large semi-amplitude of the orbital variation caused by the massive planet and the well-sampled phase curve enable a strong constraint on the orbital eccentricity.

We find that TIC 46432937 b exhibits grazing transits which in some cases can lead to a strong degeneracy between the impact parameter of the planet and the planet-to-star radius ratio. In such cases it may only be possible to provide a lower bound on the planetary radius (e.g., HATS-23 b; Bento et al. 2017). We confirmed that the Markov Chains for TIC 46432937 are well-converged and display a clear upper-limit on both the impact parameter and the planet-to-star radius ratio, so we provide best-estimates for these parameters together with two-sided uncertainties.

Figures 2–5 compare the best-fit models to the observational data. The adopted stellar parameters are listed in Table 6, while the adopted planetary parameters are listed in Table 7 and the limb darkening coefficients are listed in Table 8. In both cases we list the parameters determined assuming circular orbits.

### 3.4. *Ruling Out Blended Stellar Eclipsing Binary Scenarios*

A line-of-sight blend of three stars, including two that are eclipsing, is a relatively common false positive that can mimic the photometric transit and radial velocity signals produced by a transiting giant planet system (e.g., Torres et al. 2004). In order to rule out such an explanation for the observations of TOI 762 A or TIC 46432937 we carried out a blend analysis following the methods of Hartman et al. (2019). Here we model the photometric and astrometric data as a blend of three or more stars using the MIST version 1.2 stellar evolution models to constrain the physical properties of the stars. We consider both a hierarchical triple star system, where the two fainter stars in the system are eclipsing, and a line-of-sight blend between an eclipsing binary star system and a brighter, physically unrelated, foreground star.

For TIC 46432937 the analysis was performed before the photometric follow-up observations were available, and only the *TESS* light curves are included in this case. Because the parameters that were measured for the system when using only the *TESS* observations are fully consistent with the parameters found when incorporating the follow-up light curves from ExTrA, and as we discuss below we can already rule out blend scenarios with only the *TESS* data, we do not expect the conclusions from the blend analysis to change when incorporating the follow-up light curves. We therefore did not repeat the blend analysis for this system after obtaining the light curves from ExTrA.

For the hierarchical triple system the parameters that we vary in the fit include the times of two reference transit events, the age of the stellar system, the masses of the three stellar companions, the distance to the system, the metallicity of the system, the impact parameter of the eclipsing pair, and the limb darkening coefficients of the primary star in the eclipsing pair. For the line-of-sight blend we include all of these parameters, as well as the age, metallicity and distance of the blended foreground star. We compare both of these scenarios to a model consisting of a transiting planet around a single star for which we vary the system age, metallicity and distance, the mass and limb darkening coefficients of the host star, the impact parameter of the system, and the planet-to-star radius ratio.

For TOI 762 we also account for the 3″.2 resolved stellar companents TOI 762 A and TOI 762 B in modelling the observations, and attempt to model the brighter target TOI 762 A, for which RV variations consistent with a planetary companion were detected, as a blended system of three stars. Thus for TOI 762 there are four stars considered in the blend scenarios that we investigate, and we include the mass of the 3″.2 neighbor TOI 762 B as a

parameter in the fit, and assume that this neighbor has the same age, metallicity and distance as the brightest star in the blended object TOI 762 A.

We find that for both TOI 762 and TIC 46432937 the transiting planet scenario provides a significantly better fit to the photometric and astrometric data, with lower $\chi^2$, than the blended stellar eclipsing binary systems that we considered. For TOI 762 we find that the best-fit transiting planet model has $\Delta\chi^2 = -305$ compared to the best-fit blended eclipsing binary model, while for TIC 46432937 we find $\Delta\chi^2 = -287$. As the transiting planet scenarios also require fewer free parameters, we can confidently rule out a blended stellar eclipsing binary system for both objects. The best-fit blend scenarios exhibit secondary eclipses that are ruled out by the *TESS* observations, as well as distances and implied apparent magnitudes for the blended objects that are inconsistent with the *Gaia* parallax and measured apparent magnitudes. We therefore consider both objects to be confirmed transiting planet systems.

## 4. DISCUSSION

In this paper we presented the discovery of two transiting giant planets that orbit M dwarf stars. Fig. 6 compares these two new systems to other confirmed transiting planet systems listed in the NASA Exoplanet Archive (2024)[1]. We find that with $M_\star = 0.442 \pm 0.025\,M_\odot$, TOI 762 A is one of the lowest mass stars known to host a transiting giant planet (taking $M_p > 0.1\,M_{\rm J}$ as our definition of such a planet; it is also one of the lowest mass stars known to host a giant planet in general), while with $M_p = 3.20 \pm 0.11\,M_{\rm J}$, TIC 46432937 b is one of the highest mass planets known to transit an M dwarf star. Stars of lower mass than TOI 762 A with giant planets include TOI-4860 ($0.336\,M_\odot$; Triaud et al. 2023), TOI-519 ($0.335\,M_\odot$; Kagetani et al. 2023), TOI-5205 ($0.392\,M_\odot$; Kanodia et al. 2023), and TOI-3235 ($0.370\,M_\odot$; Hobson et al. 2023). The only transiting object orbiting an M dwarf star listed on the NASA Exoplanet Archive with a higher mass than TIC 46432937 b is TOI-1278 b (Artigau et al. 2021), but with a mass of $18.5 \pm 0.5\,M_{\rm J}$, this object may be a brown dwarf rather than a planet. The next highest mass planet is TOI-4201 b ($2.48\,M_{\rm J}$; Gan et al. 2023; Hartman et al. 2023; Delamer et al. 2023).

*Stellar Companion to TOI 762 A* —We find that TOI 762 A has a resolved stellar companion TOI 762 B. The angular separation of 3″.2 between the two stars corresponds to a current projected physical separation of 319 AU. We

---

[1] Accessed on 2024-01-17 at 12:40
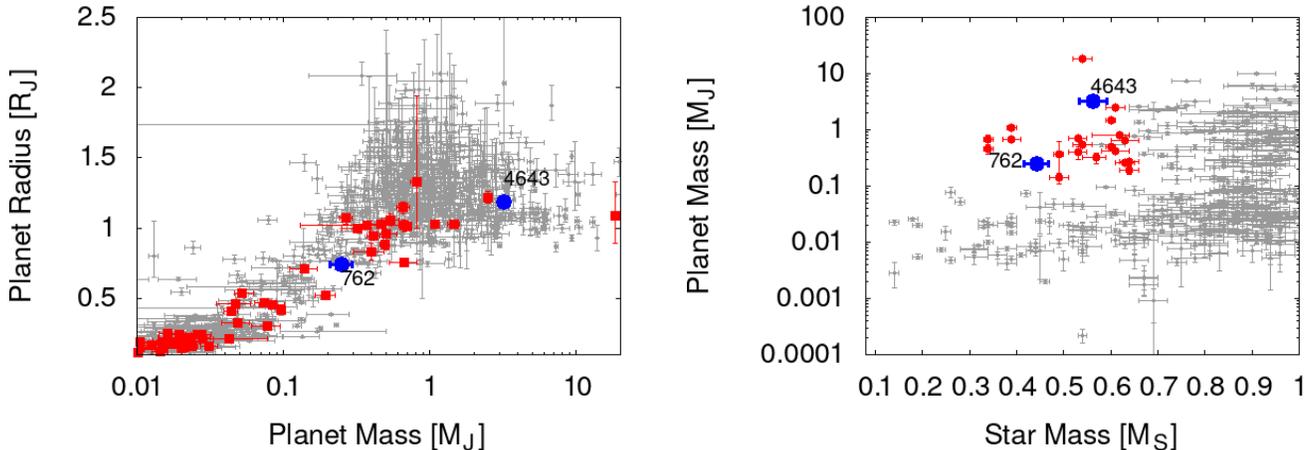
**Figure 6.** *Left:* Planet radius vs. mass. The two new planet discoveries are indicated (we abbreviate TIC 46432937 b as 4643). Small grey points show all transiting planets with measured masses and radii around K and earlier type stars from the NASA Exoplanet Archive, while red points show transiting planets with masses and radii around M dwarfs. *Right:* Planet mass vs. host star mass for transiting planets around sub-solar-mass stars. The red points in this case indicate giant planets transiting M dwarfs, while the grey points indicate other planets.

estimate that TOI 762 B has a mass of $0.227 \pm 0.010\,M_\odot$, which is 45% the mass of TOI 762 A. The eccentricity and orbital period of TOI 762 B are not known.

If the eccentricity is sufficiently high, then TOI 762 B might have induced high-eccentricity migration for the planet TOI 762 A b via the Kozai-Lidov mechanism (Kozai 1962; Lidov 1962; Naoz 2016). To get a rough sense for the time-scale of this mechanism we use eq. 7 of Kiseleva et al. (1998) assuming that the current projected physical separation corresponds to the semi-major axis of the orbit of the binary star system. We find a time-scale of $\sim 100\,\mathrm{Myr}$ if TOI 762 B has a very high eccentricity of 0.95, or $\sim 3.5\,\mathrm{Gyr}$ if the eccentricity is close to zero.

Four other M dwarfs that host transiting giant planets also have known wide stellar binary companions (TOI 3984 A, Cañas et al. 2023; TOI 5293 A, Cañas et al. 2023; TOI 3714, Cañas et al. 2022; and HATS-74 A, Jordán et al. 2022). Thus, approximately 20% of the sample of M dwarfs with transiting giant planets are known to have resolved stellar binary companions. The overall stellar multiplicity fraction for M dwarf stars is estimated to be $46 \pm 5\%$ (Susemiehl & Meyer 2022), however, a meaningful comparison to the rate for giant planet host stars will require a careful correction for observational completeness. Such a study will likely require a much larger sample of giant planet-hosting M dwarfs to enable a statistically significant result.

Ngo et al. (2016) has compared the stellar multiplicity rate for FGK stars that host hot Jupiters to the rate for field FGK stars. They find that the fraction of hot

Jupiter systems with stellar companions between 50 and 2000 AU is approximately 2.9 times the field star companion fraction. But, they also find that in the majority of cases the stellar binary companions could not drive high-eccentricity migration through the Kozai-Lidov effect. They conclude that for FGK systems, binarity is likely correlated with the formation of hot Jupiters, but the binary companions themselves do not physically drive their migration.

*High mass of TIC 46432937 b*—The high mass of TIC 46432937 b given its low stellar host mass of $0.563 \pm 0.029\,M_\odot$ poses a challenge for theories of planet formation and evolution. Gan et al. (2023) carried out interior structure modelling of the planet TOI-4201 b, which has a similar radius to TIC 46432937 b, similar host star metallicity and similar planet equilibrium temperature, but somewhat lower planet mass and somewhat larger host star mass. They find that TOI-4201 b requires a low planet bulk metal content which appears to be at odds with the high metallicity inferred for the host star. Given the higher planet mass of TIC 46432937 b, the comparably high metallicity of its host star, and the comparable planet radius and equilibrium temperature, we anticipate that a similar analysis would result in the same conclusion for TIC 46432937 b as Gan et al. (2023) arrived at for TOI-4201 b—i.e., that the planet mass/radius/equilibrium temperature requires a low planet bulk metal content that is at odds with the high host star metallicity. Gan et al. (2023) considered a variety of potential heating
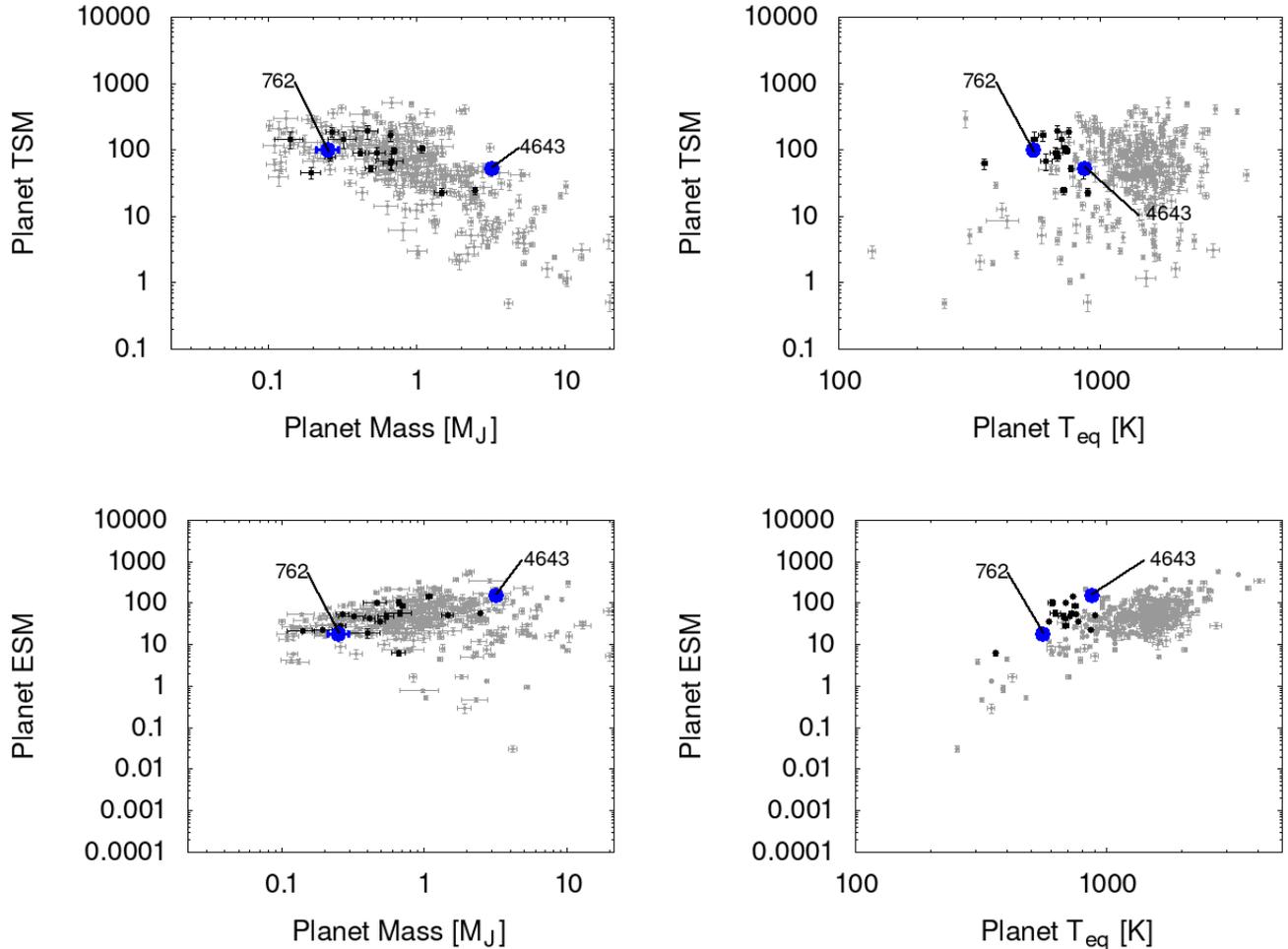
**Figure 7.**  *Top Left:* Transmission Spectroscopy Metric (TSM) vs. planet mass. TOI 762 A b and TIC 46432937 b are indicated. Small gray points show all transiting planets with measured masses $> 0.1\,M_J$ and radii $> 0.5\,R_J$ from the NASA Exoplanet Archive, while small black points denote planets with M dwarf host stars. For all panels we restrict the plots to planets for which the plotted quantities have uncertainties of less than 30%. *Top Right:* TSM vs. planet $T_{eq}$ computed assuming zero albedo and full redistribution of heat. The symbols are the same as in the left plot. *Bottom Left:* Emission Spectroscopy Metric (ESM) vs. planet mass. *Bottom Right:* ESM vs. planet $T_{eq}$. TIC 46432937 b has the highest value of TSM or ESM for a transiting warm Super-Jupiter with $M_p > 3.0\,M_J$ and $T_{eq} < 1000\,\mathrm{K}$.

sources that might explain the discrepancy, including tidal heating (Leconte et al. 2010), a gas giant merger (Li et al. 2010; Liu et al. 2015), and a more quiescent process involving an embryo being captured by a gas giant during inward migration (Lin et al. 1996). The fact that two super-Jupiter-mass planets have now been found around M dwarf stars with somewhat high radii, suggesting low bulk metal content, indicates that if there is an additional heating mechanism, it may be common for short-period giant planets around M dwarf stars. With only two planets, however, we cannot draw any definite conclusions at this point.

*Grazing Transits of TIC 46432937 b*—We find that TIC 46432937 b exhibits grazing transit events. Two other giant planets around M dwarfs have been found with grazing transits: NGTS 1 b (Bayliss et al. 2018), and the super-massive planet or brown dwarf TOI 1278 B (Artigau et al. 2021). The relatively large values of $R_p/R_\star$ for giant planets orbiting M dwarfs enhances the probability of finding these systems in grazing configurations compared to giant planets transiting Sun-like stars. The deep V-shaped transit events exhibited by these systems are often considered the hallmark of stellar eclipsing binaries, so it is important to keep in mind that transiting planets can have light

curves of this form as well when searching for giant planets transiting M dwarf stars.

Because grazing transit events do not have second or third contact points (the times when a planet starts and stops being fully in front of its host star, respectively), there is less information content in a grazing transit than in a full transit event. This can lead to degeneracies between the impact parameter and the planet-to-star radius ratio, resulting in larger uncertainties on the planetary radius and other parameters for these systems. High-precision observations, such as from *TESS*, can help break this degeneracy and enable an accurate measurement of the planetary radius in spite of the grazing transits. We find that this is the case for TIC 46432937 b, for which we find that the radius is measured to 2.5% uncertainty despite the grazing events.

One minor advantage of a grazing system is that secular variations in the orbits of these planets, due for example to the presence of exterior planets in the system, may be detectable with higher signal-to-noise than for full transits (Ribas et al. 2008). An example of this is K2-146 c, a planet whose orbit has been seen to vary between grazing and fully transiting configurations (Hamann et al. 2019). While no timing variations have been detected yet for TIC 46432937 b, the grazing transits make this an interesting target for continued transit timing observations going forward.

*Prospects for Atmospheric Characterization*—Transiting giant planets orbiting M dwarf stars can be useful objects for atmospheric characterization due to their relatively deep transits. We computed the Transmission Spectroscopy Metric and Emission Spectroscopy Metric (TSM and ESM, respectively; Kempton et al. 2018) for the two new planetary systems presented here, finding values of TSM $= 101 \pm 21$, and ESM $= 18.3 \pm 1.5$ for TOI 762 A b and TSM $= 52.3 \pm 4.8$, and ESM $= 152 \pm 11$ for TIC 46432937 b. These are compared to other transiting giant planets from the NASA Exoplanet Archive in Figure 7. While neither of the newly discovered planets has an especially high TSM value compared to the overall sample of transiting giant planets, their values are both greater than the median value of TSM $= 47.4$ for the full sample of confirmed warm transiting giant planets with equilibrium temperatures $T_{eq} < 1000$ K. When comparing against planets of $M_p > 3.0\,M_J$, the TSM of TIC 46432937 b does stand out as being greater than the value for all but four of these planets (i.e., it has a greater TSM value than 92% of all known transiting planets with $M_p > 3.0\,M_J$). These four planets (HAT-P-70 b, TSM $= 57.8$, Zhou et al. 2019; MASCARA-4 b, TSM $= 107$, Dorval et al. 2020; TOI-1431 b, TSM $=$ 109, Addison et al. 2021; and HIP 65 A b, TSM $= 780$, Nielsen et al. 2020) all have equilibrium temperatures greater than 1400 K, which is significantly higher than that of TIC 46432937 b. The next highest TSM value for a planet with $M_p > 3.0\,M_J$ and $T_{eq} < 1000$ K is 13.1 for the planet HAT-P-20 b (Bakos et al. 2011), which is a factor of four smaller than the value for TIC 46432937 b. TIC 46432937 b also has a high value of ESM for a giant planet with $T_{eq} < 1000$ K. The only giant planet that has $T_{eq} < 1000$ K and a higher ESM value than TIC 46432937 b is WASP-80 b (Triaud et al. 2013), with ESM $= 216$. WASP-80 b also has a significantly lower mass of $0.538 \pm 0.035\,M_J$. Thus TIC 46432937 b presents a particularly good opportunity for studying the atmosphere of a warm, high-mass planet. The frequent transits of this $P = 1.4404$ d system should also facilitate scheduling such observations.

*Facilities:* TESS, LCOGT, TRAPPIST, Gaia, ExTrA, SPECULOOS, VLT:ESPRESSO, Exoplanet Archive, IRSA, ZTF, ASAS-SN

*Software:* VARTOOLS (Hartman & Bakos 2016), MWDUST (Bovy et al. 2016), Astropy (Astropy Collaboration et al. 2013, 2018), ESPRESSO DRS pipeline v2.3.5 (Sosnowska et al. 2015; Modigliani et al. 2020), EsoReflex (Freudling et al. 2013), AstroImageJ (Collins et al. 2017)

## REFERENCES

Addison, B. C., Knudstrup, E., Wong, I., et al. 2021, AJ, 162, 292

Almenara, J. M., Bonfils, X., Bryant, E. M., et al. 2023, arXiv e-prints, arXiv:2308.01454

Antoniadis-Karnavas, A., Sousa, S. G., Delgado-Mena, E., et al. 2020, A&A, 636, A9

Artigau, É., Hébrard, G., Cadieux, C., et al. 2021, AJ, 162, 144

Astropy Collaboration, Robitaille, T. P., Tollerud, E. J., et al. 2013, A&A, 558, A33

Astropy Collaboration, Price-Whelan, A. M., Sipőcz, B. M., et al. 2018, AJ, 156, 123

Bakos, G. Á., Torres, G., Pál, A., et al. 2010, ApJ, 710, 1724

Bakos, G. Á., Hartman, J., Torres, G., et al. 2011, ApJ, 742, 116

Bakos, G. Á., Bayliss, D., Bento, J., et al. 2020, AJ, 159, 267

Barkaoui, K., Burdanov, A., Hellier, C., et al. 2019, AJ, 157, 43

Bayliss, D., Gillen, E., Eigmüller, P., et al. 2018, MNRAS, 475, 4467

Bensby, T., Feltzing, S., & Oey, M. S. 2014, A&A, 562, A71

Bento, J., Schmidt, B., Hartman, J. D., et al. 2017, MNRAS, 468, 835

Bonfils, X., Almenara, J. M., Jocou, L., et al. 2015, in Society of Photo-Optical Instrumentation Engineers (SPIE) Conference Series, Vol. 9605, Techniques and Instrumentation for Detection of Exoplanets VII, ed. S. Shaklan, 96051L

Borucki, W. J., Koch, D., Basri, G., et al. 2010, Science, 327, 977

Bovy, J., Rix, H.-W., Green, G. M., Schlafly, E. F., & Finkbeiner, D. P. 2016, ApJ, 818, 130

Brown, T. M., Baliber, N., Bianco, F. B., et al. 2013, PASP, 125, 1031

Bryant, E. M., Bayliss, D., & Van Eylen, V. 2023, MNRAS, 521, 3663

Burdanov, A. Y., de Wit, J., Gillon, M., et al. 2022, PASP, 134, 105001

Cañas, C. I., Stefansson, G., Kanodia, S., et al. 2020, AJ, 160, 147

Cañas, C. I., Kanodia, S., Bender, C. F., et al. 2022, AJ, 164, 50

Cañas, C. I., Kanodia, S., Libby-Roberts, J., et al. 2023, AJ, 166, 30

Caldwell, D. A., Tenenbaum, P., Twicken, J. D., et al. 2020, Research Notes of the AAS, 4, 201. https://dx.doi.org/10.3847/2515-5172/abc9b3

Choi, J., Dotter, A., Conroy, C., et al. 2016, ApJ, 823, 102

Claret, A. 2018, A&A, 618, A20

Claret, A., Hauschildt, P. H., & Witte, S. 2012, A&A, 546, A14

—. 2013, A&A, 552, A16

Cointepas, M., Almenara, J. M., Bonfils, X., et al. 2021, A&A, 650, A145

Collins, K. 2019, in American Astronomical Society Meeting Abstracts, Vol. 233, American Astronomical Society Meeting Abstracts #233, 140.05

Collins, K. A., Kielkopf, J. F., Stassun, K. G., & Hessman, F. V. 2017, AJ, 153, 77

Cutri, R. M., Wright, E. L., Conrow, T., et al. 2021, VizieR Online Data Catalog, II/328

Delamer, M., Kanodia, S., Cañas, C. I., et al. 2023, arXiv e-prints, arXiv:2307.06880

Delrez, L., Gillon, M., Queloz, D., et al. 2018, in Society of Photo-Optical Instrumentation Engineers (SPIE) Conference Series, Vol. 10700, Ground-based and Airborne Telescopes VII, ed. H. K. Marshall & J. Spyromilio, 107001I

Dorval, P., Talens, G. J. J., Otten, G. P. P. L., et al. 2020, A&A, 635, A60

Dotter, A. 2016, ApJS, 222, 8

El-Badry, K., Rix, H.-W., & Heintz, T. M. 2021, MNRAS, 506, 2269

Foreman-Mackey, D., Hogg, D. W., Lang, D., & Goodman, J. 2013, PASP, 125, 306

Freudling, W., Romaniello, M., Bramich, D. M., et al. 2013, A&A, 559, A96

Gaia Collaboration, Vallenari, A., Brown, A. G. A., et al. 2022, arXiv e-prints, arXiv:2208.00211

Gan, T., Lin, Z., Wang, S. X., et al. 2022, MNRAS, 511, 83

Gan, T., Cadieux, C., Jahandar, F., et al. 2023, AJ, 166, 165

Garcia, L. J., Timmermans, M., Pozuelos, F. J., et al. 2021, prose: FITS images processing pipeline, Astrophysics Source Code Library, record ascl:2111.006, , , ascl:2111.006

—. 2022, MNRAS, 509, 4817

Gillon, M., Jehin, E., Magain, P., et al. 2011, EPJ Web of Conferences, 11, 06002. https://doi.org/10.1051/epjconf/20101106002

Guerrero, N. M., Seager, S., Huang, C. X., et al. 2021, ApJS, 254, 39

Hamann, A., Montet, B. T., Fabrycky, D. C., Agol, E., & Kruse, E. 2019, AJ, 158, 133

Hansen, B. M. S., & Barman, T. 2007, ApJ, 671, 861

Hart, K., Shappee, B. J., Hey, D., et al. 2023, arXiv e-prints, arXiv:2304.03791

Hartman, J. D., & Bakos, G. Á. 2016, Astronomy and Computing, 17, 1

Hartman, J. D., Bayliss, D., Brahm, R., et al. 2015, AJ, 149, 166

Hartman, J. D., Bakos, G. Á., Bayliss, D., et al. 2019, AJ, 157, 55

Hartman, J. D., Jordán, A., Bayliss, D., et al. 2020, AJ, 159, 173

Hartman, J. D., Bakos, G. Á., Csubry, Z., et al. 2023, AJ, 166, 163

Hartman, Z. D., & Lépine, S. 2020, ApJS, 247, 66

Hobson, M. J., Jordán, A., Bryant, E. M., et al. 2023, ApJL, 946, L4

Howell, S. B., Everett, M. E., Sherry, W., Horch, E., & Ciardi, D. R. 2011, AJ, 142, 19

Huang, C. X., Vanderburg, A., Pál, A., et al. 2020a, Research Notes of the American Astronomical Society, 4, 204

—. 2020b, Research Notes of the American Astronomical Society, 4, 206

Jehin, E., Gillon, M., Queloz, D., et al. 2011, The Messenger, 145, 2

Jenkins, J. M. 2002, ApJ, 575, 493

Jenkins, J. M., Tenenbaum, P., Seader, S., et al. 2020, Kepler Data Processing Handbook: Transiting Planet Search, Kepler Science Document KSCI-19081-003, ,

Jenkins, J. M., Caldwell, D. A., Chandrasekaran, H., et al. 2010, ApJL, 713, L87

Jenkins, J. M., Twicken, J. D., McCauliff, S., et al. 2016, in Proc. SPIE, Vol. 9913, Software and Cyberinfrastructure for Astronomy IV, 99133E

Jensen, E. 2013, Tapir: A web interface for transit/eclipse observability, Astrophysics Source Code Library, record ascl:1306.007, , , ascl:1306.007

Johnson, J. A., Gazak, J. Z., Apps, K., et al. 2012, AJ, 143, 111

Jordán, A., Hartman, J. D., Bayliss, D., et al. 2022, AJ, 163, 125

Kagetani, T., Narita, N., Kimura, T., et al. 2023, arXiv e-prints, arXiv:2304.14703

Kanodia, S., Stefansson, G., Cañas, C. I., et al. 2021, AJ, 162, 135

Kanodia, S., Libby-Roberts, J., Cañas, C. I., et al. 2022, AJ, 164, 81

Kanodia, S., Mahadevan, S., Libby-Roberts, J., et al. 2023, AJ, 165, 120

Kempton, E. M. R., Bean, J. L., Louie, D. R., et al. 2018, PASP, 130, 114401

Kiseleva, L. G., Eggleton, P. P., & Mikkola, S. 1998, MNRAS, 300, 292

Kovács, G., Zucker, S., & Mazeh, T. 2002, A&A, 391, 369

Kozai, Y. 1962, AJ, 67, 591

Kreidberg, L. 2015, PASP, 127, 1161

Kunimoto, M., Daylan, T., Guerrero, N., et al. 2022, ApJS, 259, 33

Leconte, J., Chabrier, G., Baraffe, I., & Levrard, B. 2010, A&A, 516, A64

Li, J., Tenenbaum, P., Twicken, J. D., et al. 2019, PASP, 131, 024506

Li, S. L., Agnor, C. B., & Lin, D. N. C. 2010, ApJ, 720, 1161

Lidov, M. L. 1962, Planet. Space Sci., 9, 719

Lillo-Box, J., Figueira, P., Leleu, A., et al. 2020, A&A, 642, A121

Lin, D. N. C., Bodenheimer, P., & Richardson, D. C. 1996, Nature, 380, 606

Liu, S.-F., Agnor, C. B., Lin, D. N. C., & Li, S.-L. 2015, MNRAS, 446, 1685

Mandel, K., & Agol, E. 2002, ApJL, 580, L171

Masci, F. J., Laher, R. R., Rusholme, B., et al. 2019, PASP, 131, 018003

McQuillan, A., Mazeh, T., & Aigrain, S. 2014, ApJS, 211, 24

Modigliani, A., Freudling, W., Anderson, R. I., et al. 2020, in Astronomical Society of the Pacific Conference Series, Vol. 527, Astronomical Data Analysis Software and Systems XXIX, ed. R. Pizzo, E. R. Deul, J. D. Mol, J. de Plaa, & H. Verkouter, 667

Murray, C. A., Delrez, L., Pedersen, P. P., et al. 2020, MNRAS, 495, 2446

Naoz, S. 2016, ARA&A, 54, 441

NASA Exoplanet Archive. 2024, Planetary Systems, vVersion: 2024-01-17 12:40, NExScI-Caltech/IPAC, doi:10.26133/NEA12. https://catcopy.ipac.caltech.edu/dois/doi.php?id=10.26133/NEA12

Ngo, H., Knutson, H. A., Hinkley, S., et al. 2016, ApJ, 827, 8

Nielsen, L. D., Brahm, R., Bouchy, F., et al. 2020, A&A, 639, A76

Paxton, B., Bildsten, L., Dotter, A., et al. 2011, ApJS, 192, 3

Paxton, B., Cantiello, M., Arras, P., et al. 2013, ApJS, 208, 4

Paxton, B., Marchant, P., Schwab, J., et al. 2015, ApJS, 220, 15

Pepe, F., Cristiani, S., Rebolo, R., et al. 2021, A&A, 645, A96

Popinchalk, M., Faherty, J. K., Kiman, R., et al. 2021, ApJ, 916, 77

Ribas, I., Font-Ribera, A., & Beaulieu, J.-P. 2008, ApJL, 677, L59

Ricker, G. R., Winn, J. N., Vanderspek, R., et al. 2015, Journal of Astronomical Telescopes, Instruments, and Systems, 1, 014003

Riello, M., De Angeli, F., Evans, D. W., et al. 2021, A&A, 649, A3

Schönrich, R., Binney, J., & Dehnen, W. 2010, MNRAS, 403, 1829

Scott, N. J., Howell, S. B., Gnilka, C. L., et al. 2021, Frontiers in Astronomy and Space Sciences, 8, 138

Sebastian, D., Gillon, M., Ducrot, E., et al. 2021, A&A, 645, A100

Shappee, B. J., Prieto, J. L., Grupe, D., et al. 2014, ApJ, 788, 48

Skrutskie, M. F., Cutri, R. M., Stiening, R., et al. 2006, AJ, 131, 1163

Smith, J. C., Stumpe, M. C., Van Cleve, J. E., et al. 2012, PASP, 124, 1000

Sosnowska, D., Lovis, C., Figueira, P., et al. 2015, in Astronomical Society of the Pacific Conference Series, Vol. 495, Astronomical Data Analysis Software an Systems XXIV (ADASS XXIV), ed. A. R. Taylor & E. Rosolowsky, 285

Stumpe, M. C., Smith, J. C., Catanzarite, J. H., et al. 2014, PASP, 126, 100

Stumpe, M. C., Smith, J. C., Van Cleve, J. E., et al. 2012, PASP, 124, 985

Susemiehl, N., & Meyer, M. R. 2022, A&A, 657, A48

Tayar, J., Claytor, Z. R., Huber, D., & van Saders, J. 2022, ApJ, 927, 31

Torres, G., Konacki, M., Sasselov, D. D., & Jha, S. 2004, ApJ, 614, 979

Triaud, A. H. M. J., Anderson, D. R., Collier Cameron, A., et al. 2013, A&A, 551, A80

Triaud, A. H. M. J., Dransfield, G., Kagetani, T., et al. 2023, MNRAS, 525, L98

Twicken, J. D., Catanzarite, J. H., Clarke, B. D., et al. 2018, PASP, 130, 064502

Zacharias, N., Finch, C. T., Girard, T. M., et al. 2013, AJ, 145, 44

Zechmeister, M., & Kürster, M. 2009, A&A, 496, 577

Zhou, G., Huang, C. X., Bakos, G. Á., et al. 2019, AJ, 158, 141

**Table 4.** Astrometric, Spectroscopic and Photometric parameters for TOI 762 A and TIC 46432937

| Parameter | TOI 762 A Value | TIC 46432937 Value | Source |
|---|---|---|---|
| Astrometric properties and cross-identifications | | | |
| 2MASS-ID................................. | 11041818-4749169 | 05352856-1435504 | |
| TIC-ID.................................... | 178709444 | 46432937 | |
| TOI-ID.................................... | 762 | $\cdots$ | |
| GAIA DR2-ID............................. | 5362352744504000256 | 2984391358868786816 | |
| R.A. (J2000) ............................. | $11^h 04^m 18.1831s$ | $05^h 35^m 28.5693s$ | GAIA DR3 |
| Dec. (J2000) ............................. | $-47° 49' 17.0030''$ | $-14° 35' 50.4600''$ | GAIA DR3 |
| $\mu_{R.A.}$ (mas yr$^{-1}$) | $-159.174 \pm 0.020$ | $-13.365 \pm 0.013$ | GAIA DR3 |
| $\mu_{Dec.}$ (mas yr$^{-1}$) | $-24.780 \pm 0.020$ | $36.962 \pm 0.012$ | GAIA DR3 |
| parallax (mas) | $10.118 \pm 0.023$ | $11.031 \pm 0.013$ | GAIA DR3 |
| Spectroscopic properties | | | |
| $T_{eff\star}$ (K) ................................ | $3150 \pm 67$ | $3535 \pm 65$ | see Section 3.1 |
| [Fe/H].................................... | $0.24 \pm 0.10$ | $0.03 \pm 0.10$ | see Section 3.1 |
| $\gamma_{RV}$ (m s$^{-1}$) ............................. | $48680.1 \pm 4.3$ | $102279.1 \pm 2.5$ | ESPRESSO |
| Photometric properties[a] | | | |
| $G$ (mag)[b] ................................ | $14.9297 \pm 0.0028$ | $13.4172 \pm 0.0028$ | GAIA DR3 |
| $BP$ (mag)[b] ............................. | $\cdots$ | $14.4962 \pm 0.0033$ | GAIA DR3 |
| $RP$ (mag)[b] ............................. | $\cdots$ | $12.3785 \pm 0.0039$ | GAIA DR3 |
| $B$ (mag)................................. | $\cdots$ | $15.707 \pm 0.050$ | APASS[c] |
| $V$ (mag)................................. | $\cdots$ | $14.310 \pm 0.020$ | APASS[c] |
| $g$ (mag) ................................. | $\cdots$ | $15.040 \pm 0.060$ | APASS[c] |
| $r$ (mag) ................................. | $\cdots$ | $13.740 \pm 0.020$ | APASS[c] |
| $i$ (mag) ................................. | $\cdots$ | $12.792 \pm 0.040$ | APASS[c] |
| $J$ (mag)[d] ................................ | $12.099 \pm 0.080$ | $11.011 \pm 0.022$ | 2MASS |
| $H$ (mag)[d] ................................ | $11.444 \pm 0.077$ | $10.427 \pm 0.023$ | 2MASS |
| $K_s$ (mag)[d] ................................ | $11.187 \pm 0.082$ | $10.195 \pm 0.020$ | 2MASS |
| $W1$ (mag)[e] ............................... | $10.991 \pm 0.088$ | $10.114 \pm 0.023$ | WISE |
| $W2$ (mag)[e] ............................... | $10.890 \pm 0.094$ | $10.063 \pm 0.020$ | WISE |
| $W3$ (mag)[e] ............................... | $10.71 \pm 0.12$ | $9.910 \pm 0.055$ | WISE |

[a] We only include in the table catalog magnitudes that were included in our analysis of each system.

[b] The listed uncertainties for the Gaia DR3 photometry are taken from the catalog. For the analysis we assume an additional systematic uncertainty of 0.02 mag for all bandpasses.

[c] From APASS DR6 as listed in the UCAC 4 catalog (Zacharias et al. 2013). Although these measurements are also available for TOI 762 A, we do not include them in the analysis or list them here because the degree to which these measurements are contaminated by flux from the 3''.2 and 4''.7 neighbors is difficult to determine.

[d] From the 2MASS catalog (Skrutskie et al. 2006). For TOI 762 A we subtracted an estimate for the flux contribution from TOI 762 B.

[e] From the 2021 Feb 16 ALLWISE Data release of the WISE mission (Cutri et al. 2021). For TOI 762 A we subtracted an estimate for the flux contribution from TOI 762 B.

**Table 5**. ESPRESSO radial velocities for TOI 762 A and TIC 46432937.

| System | BJD (2,450,000+) | RV[a] (m s$^{-1}$) | $\sigma_{RV}$[b] (m s$^{-1}$) | Phase (m s$^{-1}$) | Instrument[c] |
|---|---|---|---|---|---|
| TOI-762 | 8818.82472 | 47.93 | 11.30 | 0.901 | ESPRESSO/P104 |
| TOI-762 | 8822.81705 | $-17.07$ | 11.50 | 0.051 | ESPRESSO/P104 |
| TOI-762 | 8836.78307 | $-29.07$ | 8.70 | 0.074 | ESPRESSO/P104 |
| TOI-762 | 8839.83846 | 19.93 | 5.80 | 0.954 | ESPRESSO/P104 |
| TOI-762 | 8841.81658 | 4.93 | 6.40 | 0.524 | ESPRESSO/P104 |

*Table 5 continued*

**Table 5** *(continued)*

| System | BJD | RV[a] | $\sigma_{RV}$[b] | Phase | Instrument[c] |
|---|---|---|---|---|---|
| | (2,450,000+) | (m s$^{-1}$) | (m s$^{-1}$) | (m s$^{-1}$) | |
| TOI-762 | 9938.80622 | 3.43 | 7.14 | 0.506 | ESPRESSO/P110 |
| TOI-762 | 9942.74132 | 39.13 | 10.60 | 0.639 | ESPRESSO/P110 |
| TOI-762 | 9943.75858 | 40.13 | 8.42 | 0.932 | ESPRESSO/P110 |
| TIC-46432937 | 9907.75857 | −423.38 | 1.95 | 0.086 | ESPRESSO |
| TIC-46432937 | 9909.74414 | −187.38 | 2.49 | 0.464 | ESPRESSO |
| TIC-46432937 | 9928.64212 | 417.62 | 3.81 | 0.584 | ESPRESSO |
| TIC-46432937 | 9930.76066 | −277.38 | 1.94 | 0.054 | ESPRESSO |
| TIC-46432937 | 9936.72836 | −797.38 | 1.81 | 0.197 | ESPRESSO |
| TIC-46432937 | 9995.60029 | −336.38 | 3.53 | 0.068 | ESPRESSO |
| TIC-46432937 | 9996.56963 | 836.62 | 2.08 | 0.741 | ESPRESSO |
| TIC-46432937 | 9997.63070 | −122.38 | 1.97 | 0.478 | ESPRESSO |

[a] The zero-point of these velocities is arbitrary. An overall offset $\gamma_{\rm rel}$ fitted to the orbit has been subtracted for each system.

[b] Internal errors excluding the component of astrophysical jitter allowed to vary in the fit.

[c] For TOI 762 A we distinguish between the ESPRESSO observations obtained during P104 and those obtained during P110 for which we allow independent zero-point offsets in the fit.

**Table 6.** Adopted derived stellar parameters for TOI 762 A and TIC 46432937.

| | TOI 762 A | TIC 46432937 |
|---|---|---|
| Parameter | Value | Value |
| $M_\star$ ($M_\odot$) ........ | $0.442 \pm 0.025$ | $0.563 \pm 0.029$ |
| $R_\star$ ($R_\odot$) ........ | $0.4250 \pm 0.0091$ | $0.5299 \pm 0.0091$ |
| $\log g_\star$ (cgs) ....... | $4.827 \pm 0.010$ | $4.740 \pm 0.010$ |
| $\rho_\star$ ($\mathrm{g\,cm}^{-3}$) ...... | $8.11 \pm 0.20$ | $5.34 \pm 0.11$ |
| $L_\star$ ($L_\odot$) .......... | $0.0185 \pm 0.0011$ | $0.0412 \pm 0.0031$ |
| $T_{\mathrm{eff}\star}$ (K) ........ | $3266 \pm 36$ | $3572 \pm 57$ |
| [Fe/H] ........... | $0.357 \pm 0.085$ | $0.323 \pm 0.081$ |
| Age (Gyr) ........ | $9.3 \pm 5.5$ | $7.4 \pm 5.1$ |
| $A_V$ (mag) ........ | $0.1740 \pm 0.0052$ | $0.023 \pm 0.012$ |
| Distance (pc) ..... | $98.78 \pm 0.22$ | $90.64 \pm 0.10$ |

NOTE— The listed parameters are those determined through the joint differential evolution Markov Chain analysis, including systematic errors in the stellar evolution models, described in Section 3.3. For all systems the RV observations are consistent with a circular orbit, and we assume a fixed circular orbit in generating the parameters listed here.

**Table 7.** Adopted orbital and planetary parameters for TOI 762 A b, and TIC 46432937 b

| Parameter | TOI 762 A b Value | TIC 46432937 b Value |
|---|---|---|
| Light curve parameters | | |
| $P$ (days) ......................... | $3.47168260 \pm 0.00000072$ | $1.440445270 \pm 0.000000087$ |
| $T_c$ (BJD_TDB) [a] .............. | $2459850.258470 \pm 0.000094$ | $2459952.288940 \pm 0.000039$ |
| $T_{14}$ (days) [a] .................... | $0.05789 \pm 0.00031$ | $0.04981 \pm 0.00026$ |
| $T_{12} = T_{34}$ (days) [a] ............. | $0.01877 \pm 0.00048$ | $\cdots$ |
| $\phi_{\mathrm{occ}}$ (phase) [b] ................. | $0.513 \pm 0.018$ | $0.50064 \pm 0.00093$ |
| $T_{c,\mathrm{occ}}$ (BJD_TDB) [b] .......... | $2459876.341 \pm 0.062$ | $2460009.1874 \pm 0.0013$ |
| $T_{14,\mathrm{occ}}$ (days) [b] .............. | $0.05759 \pm 0.00067$ | $0.05237 \pm 0.00073$ |
| $a/R_\star$ .......................... | $17.29 \pm 0.14$ | $8.381 \pm 0.056$ |
| $\zeta/R_\star$ [c] ........................ | $47.79 \pm 0.30$ | $64.73^{+2.37}_{-0.89}$ |
| $R_p/R_\star$ ........................ | $0.17985 \pm 0.00095$ | $0.2301 \pm 0.0037$ |
| $b^2$ ............................ | $0.5710^{+0.0086}_{-0.0101}$ | $0.681^{+0.026}_{-0.012}$ |
| $b \equiv a\cos i/R_\star$ ................. | $0.7556^{+0.0057}_{-0.0067}$ | $0.8250^{+0.0157}_{-0.0073}$ |
| $i$ (deg) ......................... | $87.500 \pm 0.039$ | $84.350^{+0.090}_{-0.140}$ |
| RV parameters | | |
| $K$ (m s$^{-1}$) ..................... | $58.1 \pm 9.3$ | $837.1 \pm 4.4$ |
| $e$ [d] ........................... | $< 0.083$ | $< 0.009$ |
| RV jitter ESPRESSO 1[e] (m s$^{-1}$) | $0.1 \pm 4.1$ | $5.3 \pm 2.5$ |
| RV jitter ESPRESSO 2[e] (m s$^{-1}$) | $0.0 \pm 2.9$ | $\cdots$ |
| Planetary parameters | | |
| $M_p$ ($M_{\mathrm{J}}$) ..................... | $0.251 \pm 0.042$ | $3.20 \pm 0.11$ |
| $R_p$ ($R_{\mathrm{J}}$) ..................... | $0.744 \pm 0.017$ | $1.188 \pm 0.030$ |
| $C(M_p, R_p)$ [f] .................. | $0.17$ | $0.53$ |
| $\rho_p$ (g cm$^{-3}$) ................... | $0.76 \pm 0.13$ | $2.37 \pm 0.15$ |
| $\log g_p$ (cgs) .................... | $3.053 \pm 0.072$ | $3.751^{+0.016}_{-0.023}$ |
| $a$ (AU) ......................... | $0.03418 \pm 0.00065$ | $0.02065 \pm 0.00035$ |
| $T_{\mathrm{eq}}$ (K) ......................... | $555.4 \pm 6.4$ | $872 \pm 14$ |
| $\Theta$ [g] ............................ | $0.0523 \pm 0.0085$ | $0.1951 \pm 0.0051$ |
| $\log_{10}\langle F \rangle$ (cgs) [h] ............... | $7.334 \pm 0.020$ | $8.119 \pm 0.028$ |

NOTE— For both systems we adopt a model in which the orbit is assumed to be circular. Except where noted otherwise, the listed parameters are calculated assuming circular orbits. See the discussion in Section 3.3.

[a] Times are in Barycentric Julian Date calculated on the Barycentric Dynamical Time (TDB) system. $T_c$: Reference epoch of mid transit that minimizes the correlation with the orbital period. $T_{14}$: total transit duration, time between first to last contact; $T_{12} = T_{34}$: ingress/egress time, time between first and second, or third and fourth contact.

[b] Inferred timing of occultation events calculated from the fit where the eccentricity is allowed to vary. Occultations have not been observed for either system. Times are in Barycentric Julian Date calculated on the Barycentric Dynamical Time (TDB) system. $\phi_{\mathrm{occ}}$: orbital phase of the occultation. Phase 0 refers to the time of mid transit. $T_{c,\mathrm{occ}}$: Reference epoch of mid occultation. $T_{14,\mathrm{occ}}$: total occultation duration.

[c] Reciprocal of the half duration of the transit used as a jump parameter in our MCMC analysis in place of $a/R_\star$. It is related to $a/R_\star$ by the expression $\zeta/R_\star = a/R_\star(2\pi(1 + e\sin\omega))/(P\sqrt{1 - b^2}\sqrt{1 - e^2})$ (Bakos et al. 2010).

[d] The 95% confidence upper limit on the eccentricity determined when $\sqrt{e}\cos\omega$ and $\sqrt{e}\sin\omega$ are allowed to vary in the fit.

[e] Term added in quadrature to the formal RV uncertainties for each instrument. This is treated as a free parameter in the fitting routine. The two values listed for TOI 762 A b are for the ESPRESSO P104 and P110 data, respectively.

[f] Correlation coefficient between the planetary mass $M_p$ and radius $R_p$ estimated from the posterior parameter distribution.

[g] The Safronov number is given by $\Theta = \frac{1}{2}(V_{\mathrm{esc}}/V_{\mathrm{orb}})^2 = (a/R_p)(M_p/M_\star)$ (see Hansen & Barman 2007).

[h] Incoming flux per unit surface area, averaged over the orbit.

**Table 8.** Adopted limb darkening coefficients for TOI 762 A b, and TIC 46432937 b

|  | TOI 762 A b | TIC 46432937 b |
|---|---|---|
| Parameter | Value | Value |
| $c_1, g$ ......................... | $0.65 \pm 0.14$ | $\cdots$ |
| $c_2, g$ ......................... | $0.09 \pm 0.16$ | $\cdots$ |
| $c_1, r$ ......................... | $0.44 \pm 0.14$ | $\cdots$ |
| $c_2, r$ ......................... | $0.30 \pm 0.17$ | $\cdots$ |
| $c_1, i$ ......................... | $0.23 \pm 0.12$ | $\cdots$ |
| $c_2, i$ ......................... | $0.13 \pm 0.15$ | $\cdots$ |
| $c_1, zs$ ......................... | $0.13 \pm 0.11$ | $\cdots$ |
| $c_2, zs$ ......................... | $0.10 \pm 0.12$ | $\cdots$ |
| $c_1, I+z$ ...................... | $0.37 \pm 0.15$ | $\cdots$ |
| $c_2, I+z$ ...................... | $0.28^{+0.14}_{-0.19}$ | $\cdots$ |
| $c_1, Z$ ......................... | $\cdots$ | $0.143 \pm 0.096$ |
| $c_2, Z$ ......................... | $\cdots$ | $0.15 \pm 0.14$ |
| $c_1, Y$ ......................... | $\cdots$ | $0.108^{+0.097}_{-0.071}$ |
| $c_2, Y$ ......................... | $\cdots$ | $0.06 \pm 0.12$ |
| $c_1, J$ ......................... | $\cdots$ | $0.142 \pm 0.088$ |
| $c_2, J$ ......................... | $\cdots$ | $0.09 \pm 0.13$ |
| $c_1, H$ ......................... | $\cdots$ | $0.20 \pm 0.11$ |
| $c_2, H$ ......................... | $\cdots$ | $0.08 \pm 0.15$ |
| $c_1, z-H$ ...................... | $0.050^{+0.066}_{-0.037}$ | $\cdots$ |
| $c_2, z-H$ ...................... | $-0.000 \pm 0.071$ | $\cdots$ |
| $c_1, T$ ......................... | $0.132 \pm 0.091$ | $0.20 \pm 0.10$ |
| $c_2, T$ ......................... | $0.02 \pm 0.13$ | $0.17 \pm 0.14$ |

NOTE— For all systems we adopt a model in which the orbit is assumed to be circular. See the discussion in Section 3.3. The values listed are for a quadratic law. The limb darkening parameters were directly varied in the fit, using the tabulations from Claret et al. (2012, 2013); Claret (2018) to place Gaussian prior constraints on their values, assuming a prior uncertainty of 0.2 for each coefficient.